Computers and Fluids 294 (2025) 106622

Contents lists available at ScienceDirect

Computers and Fluids

journal homepage: www.elsevier.com/locate/compfluid

Locally energy-stable finite element schemes for incompressible flow problems: Design and analysis for equal-order interpolations

Hennes Hajduk [a], Dmitri Kuzmin [b,*], Gert Lube [c], Philipp Öffner [d]

[a] Department of Geosciences, University of Oslo, Postboks 1022 Blindern, 0315 Oslo, Norway
[b] Institute of Applied Mathematics (LS III), TU Dortmund University, Vogelpothsweg 87, D-44227 Dortmund, Germany
[c] Institute for Numerical and Applied Mathematics, Georg-August-Universität Göttingen, D-37083 Göttingen, Germany
[d] Department of Mathematics, TU Clausthal, Erzstraße 1, D-38678 Clausthal-Zellerfeld, Germany

ARTICLE INFO

Keywords:
Incompressible Euler and Navier–Stokes equations
Stabilized finite element methods
Equal-order interpolation
Energy inequality
Consistency
Convergence
Dissipative weak solutions

ABSTRACT

We show that finite element discretizations of incompressible flow problems can be designed to ensure preservation/dissipation of kinetic energy not only globally but also locally. In the context of equal-order (piecewise-linear) interpolations, we prove the validity of a semi-discrete energy inequality for a quadrature-based approximation to the nonlinear convective term, which we combine with the Becker–Hansbo pressure stabilization. An analogy with entropy-stable algebraic flux correction schemes for the compressible Euler equations and the shallow water equations yields a weak 'bounded variation' estimate from which we deduce the semi-discrete Lax–Wendroff consistency and convergence towards dissipative weak solutions. The results of our numerical experiments for standard test problems confirm that the method under investigation is non-oscillatory and exhibits optimal convergence behavior.

1. Introduction

High-resolution schemes for nonlinear systems of conservation laws are typically based on generalizations of algorithms originally designed to ensure strong stability in the case of a scalar equation [1]. Prominent representatives of such approaches include multidimensional flux-corrected transport (FCT) methods [2–4] and local extremum diminishing (LED) alternatives [5–7]. A common drawback of straightforward extensions to systems is the lack of rigorous theoretical justification. For example, many FCT and LED schemes for the compressible Euler equations produce essentially non-oscillatory approximations but do not guarantee positivity preservation or entropy stability.

The design and analysis of structure-preserving numerical methods for compressible flow problems have gained momentum in recent years. In particular, provably invariant domain preserving, entropy stable, and kinetic energy preserving finite volume schemes were proposed in the literature [8–16]. Modern approaches to algebraic flux correction [2,17] for finite element methods were designed to enforce preservation of invariant domains (positivity preservation) [18–21], local discrete maximum principles for scalar quantities of interest [22,23], and entropy stability conditions [24–26]. Subcell limiting techniques based on these criteria were designed in [27–31] for high-order finite elements. Feireisl et al. [32,33] introduced a general framework for proving convergence of structure-preserving schemes to dissipative measure-valued solutions of multidimensional hyperbolic systems under the assumptions of uniform boundedness and entropy stability. Examples of finite element analysis based on this theory can be found in [34–36].

Numerical schemes for incompressible flow problems often use stabilization terms to prevent spurious oscillations in the velocity and pressure fields. It is essential to ensure that these terms suppress numerical instabilities, while preserving fine-scale features of physical origin. In the context of monotonically integrated large eddy simulation (MILES) of turbulent incompressible flows, numerical viscosity of an FCT-like discretization method serves as an implicit subgrid scale (SGS) model for unresolvable effects [37–41]. As explained in [42,43], the kinetic energy preservation (KEP) property of discretized advection terms is an essential requirement for realistic SGS modeling of the energy cascade. The KEP design criterion dictates the use of (skew-)symmetry preserving discretization methods [44,45]. Failure to ensure consistency with the local energy equations presented in [43,46] may result in numerical artifacts or instabilities. Many finite element methods for the incompressible Euler and Navier–Stokes equations guarantee global energy stability. However, we are not aware of any finite element method that is locally energy stable in the sense that a (semi-)discrete

* Corresponding author.
E-mail addresses: hennes.hajduk@geo.uio.no (H. Hajduk), kuzmin@math.uni-dortmund.de (D. Kuzmin), lube@math.uni-goettingen.de (G. Lube), mail@philippoeffner.de (P. Öffner).

https://doi.org/10.1016/j.compfluid.2025.106622
Received 8 October 2024; Received in revised form 24 January 2025; Accepted 28 March 2025
Available online 9 April 2025
0045-7930/© 2025 The Authors. Published by Elsevier Ltd. This is an open access article under the CC BY license (http://creativecommons.org/licenses/by/4.0/).

energy inequality holds for the nodal values. In our proofs of consistency, we use this particular energy stability property to derive a weak BV bound (cf. [35,47]) and show that the uniform boundedness of nodal velocities and pressures implies that of nodal accelerations. The local energy inequality formulated in [48, Thm. 2] is an interesting theoretical result but it does not provide the estimates that we need.

According to Fehn et al. [49, Sec. 7], the question of whether or not local energy stability is a prerequisite for weak convergence requires further investigations. As a first step towards that end, we adapt the algebraic flux correction (AFC) tools developed in [1,20,25,50] and the analysis carried out in [32,33,35,36] to continuous $\mathbb{P}_1\mathbb{P}_1$ finite element discretizations of the Navier–Stokes system. The velocity is stabilized using a structure-preserving quadrature rule. Checkerboard pressure modes are avoided using the stabilization proposed in [51]. In contrast to standard analysis of finite element methods for the incompressible Navier–Stokes equations, we do not assume continuity or regularity of exact solutions. Our theoretical studies build on the work of Duchon and Robert [46] and Székelyhidi Jr. and Wiedemann [52]. We are interested in analyzing the limit of vanishing viscosity and gaining deeper insight into the behavior of dissipative weak solutions to incompressible flow problems.

For a spectral (viscosity) method [53,54] and a first-order asymptotically preserving staggered grid finite volume (FV) scheme [55], it was recently demonstrated that dissipative measure-valued (DMV) solutions of the compressible system converge to the DMV solutions of the incompressible system as the Mach number and the mesh size tend to zero. Further recent efforts in the field of numerical analysis were focused on incorporating stochastic noise into deterministic flow models to improve the regularity and provide a more realistic modeling of turbulence effects. These studies employ more general solution concepts, such as dissipative measure-valued martingale solutions or weak pathwise solutions, demonstrating their existence through the convergence of consistent numerical schemes and/or providing error estimates; see [56–58] and references cited therein. A common feature of existing proof techniques for deterministic and stochastic models is the use of divergence-free test functions. To the best of the authors' knowledge, no direct proofs of convergence to generalized solutions are available for equal-order interpolations, such as the $\mathbb{P}_1\mathbb{P}_1$ finite element pairs considered in our work.

The remainder of this paper is organized as follows. In Section 2, we present our finite element method. In Section 3, we prove local energy stability and consistency under the assumption of strong convergence. Weak-$*$ convergence to dissipative weak solutions is shown in Section 4. The numerical examples of Section 5 demonstrate that the proposed scheme is, indeed, non-oscillatory and achieves optimal convergence rates. The results are discussed and conclusions are drawn in Section 6.

2. Stabilized finite element method

Let $\Omega \subset \mathbb{R}^d$, $d \in \{2,3\}$ be a bounded domain. The Navier–Stokes equations for the velocity $\mathbf{u}(\mathbf{x},t)$ and pressure $p(\mathbf{x},t)$ of an incompressible fluid can be written in the skew-symmetric form

$$\frac{\partial \mathbf{u}}{\partial t} + \frac{1}{2}[\nabla\cdot(\mathbf{u}\otimes\mathbf{u}) + \mathbf{u}\cdot\nabla\mathbf{u}] + \nabla p = \nu\Delta\mathbf{u} \qquad \text{in } \Omega\times(0,\infty), \tag{1a}$$

$$\nabla\cdot\mathbf{u} = 0 \qquad \text{in } \Omega\times(0,\infty). \tag{1b}$$

The kinematic viscosity $\nu \geq 0$ is assumed to be constant. In the case $\nu = 0$, the general Navier–Stokes system (1) reduces to the incompressible Euler equations. We prescribe the initial condition

$$\mathbf{u}(\cdot,0) = \mathbf{u}_0 \qquad \text{in } \Omega, \tag{2}$$

where $\mathbf{u}_0$ is a given solenoidal vector field. To avoid distinguishing between the viscous and inviscid flow regimes, we impose periodic boundary conditions on the boundary $\Gamma = \partial\Omega$. Since the pressure is defined up to a constant in the periodic case, we require that $\int_\Omega p(\mathbf{x},t)\,\mathrm{d}\mathbf{x} = 0$ for $t > 0$.

If $\mathbf{u}$ is a smooth exact solution to (1), then the specific kinetic energy $\eta(\mathbf{u}) = \frac{|\mathbf{u}|^2}{2}$ satisfies (cf. [46])

$$\frac{\partial \eta(\mathbf{u})}{\partial t} + \nabla\cdot\mathbf{q}(\mathbf{u},p) \leq 0 \qquad \text{in } \Omega\times(0,\infty), \tag{3}$$

where $\mathbf{q}(\mathbf{u},p) = (\eta(\mathbf{u}) + p)\mathbf{u}$. It follows that $\int_\Omega \eta(\mathbf{u}(\mathbf{x},t))\,\mathrm{d}\mathbf{x}$ is a non-increasing function of $t \geq 0$.

2.1. Galerkin space discretization

We discretize (1) in space using the $\mathbb{P}_1\mathbb{P}_1$ finite element pair[1] on a conforming simplex mesh $\mathcal{T}_h$. The scalar Lagrange basis functions associated with its vertices $\mathbf{x}_1,\dots,\mathbf{x}_{N_h}$ are denoted by $\varphi_1,\dots,\varphi_{N_h}$. They span a finite element space V_h, are nonnegative, and have the *partition-of-unity* property

$$\sum_{j=1}^{N_h}\varphi_j(\mathbf{x}) = 1 \qquad \forall\mathbf{x}\in\bar{\Omega}. \tag{4}$$

Inserting the continuous finite element approximations

$$\mathbf{u}_h(\mathbf{x},t) = \sum_{j=1}^{N_h}\mathbf{u}_j(t)\varphi_j(\mathbf{x}), \qquad p_h(\mathbf{x},t) = \sum_{k=1}^{N_h}p_k(t)\varphi_k(\mathbf{x}) \tag{5}$$

into the skew-symmetric Galerkin weak form

$$\int_\Omega\left(\frac{\partial\mathbf{u}_h}{\partial t} + \frac{1}{2}[\nabla\cdot(\mathbf{u}_h\otimes\mathbf{u}_h) + \mathbf{u}_h\cdot\nabla\mathbf{u}_h] + \nabla p_h\right)\cdot\mathbf{v}_h\,\mathrm{d}\mathbf{x} + \nu\int_\Omega\nabla\mathbf{u}_h : \nabla\mathbf{v}_h\,\mathrm{d}\mathbf{x} = 0, \tag{6a}$$

$$-\int_\Omega(\nabla\cdot\mathbf{u}_h)q_h\,\mathrm{d}\mathbf{x} = 0 \tag{6b}$$

of system (1) with vector-valued velocity test functions $\mathbf{v}_h \in \mathbf{V}_h := (V_h)^d$ and scalar-valued pressure test functions $q_h \in V_h$, we obtain a spatial semi-discretization that can be written as

$$\sum_{j\in\mathcal{N}_i}\left(m_{ij}\frac{\mathrm{d}\mathbf{u}_j}{\mathrm{d}t}\right) = -\sum_{j\in\mathcal{N}_i}[(a_{ij}+\nu s_{ij})\mathbf{u}_j + \mathbf{c}_{ij}p_j], \qquad i = 1,\dots,N_h, \tag{7a}$$

$$0 = -\sum_{j\in\mathcal{N}_k}\mathbf{c}_{kj}\cdot\mathbf{u}_j, \qquad k = 1,\dots,N_h. \tag{7b}$$

We denote by $\mathcal{N}_i$ the set of node indices j such that the basis functions φ_i and φ_j have overlapping supports. The constant coefficients of the semi-discrete problem (7) are defined by

$$m_{ij} = \int_\Omega\varphi_i\varphi_j\,\mathrm{d}\mathbf{x}, \qquad \mathbf{c}_{ij} = \int_\Omega\varphi_i\nabla\varphi_j\,\mathrm{d}\mathbf{x}, \qquad s_{ij} = \int_\Omega\nabla\varphi_i\cdot\nabla\varphi_j\,\mathrm{d}\mathbf{x}. \tag{8}$$

The entries

$$a_{ij} = \frac{1}{2}\int_\Omega[\varphi_i\mathbf{u}_h\cdot\nabla\varphi_j - \varphi_j\mathbf{u}_h\cdot\nabla\varphi_i]\,\mathrm{d}\mathbf{x} \tag{9}$$

of the discrete convection operator depend on $\mathbf{u}_h$. It is easy to verify that

$$m_{ij} = m_{ji}, \qquad \mathbf{c}_{ij} = -\mathbf{c}_{ji}, \qquad s_{ij} = s_{ji}, \qquad a_{ij} = -a_{ji}. \tag{10}$$

Remark 1. If non-periodic boundary conditions are imposed on Γ, then

$$\mathbf{c}_{ij} = -\mathbf{c}_{ji} + \int_\Gamma\varphi_i\varphi_j\mathbf{n}\,\mathrm{d}s,$$

and the equations associated with boundary nodes need to be eliminated or modified (see, e.g., [59]).

[1] In Section 5, we also show numerical results obtained with $\mathbb{Q}_1\mathbb{Q}_1$ approximations on quadrilateral meshes.

In the case of non-vanishing viscosity $\nu > 0$, we assume that the mesh $\mathcal{T}_h$ satisfies the geometric angle conditions under which $s_{ij} \le 0$ for $j \neq i$ (see, e.g., [60]). From (4) we deduce that

$$\sum_{j=1}^{N_h} \mathbf{c}_{ij} = \mathbf{0}, \qquad \sum_{j=1}^{N_h} s_{ij} = 0, \qquad \sum_{j=1}^{N_h} a_{ij} = -\frac{1}{2}\int_\Omega \mathbf{u}_h \cdot \nabla\varphi_i \,\mathrm{d}\mathbf{x}. \tag{11}$$

Remark 2. Substituting $\mathbf{v}_h = \mathbf{u}_h$ and $q_h = p_h$ into (6), we obtain the evolution equation

$$\begin{aligned}\frac{\mathrm{d}}{\mathrm{d}t}\int_\Omega \eta(\mathbf{u}_h)\,\mathrm{d}\mathbf{x} &= -\frac{1}{2}\int_\Omega \big[\nabla\cdot(\mathbf{u}_h\otimes\mathbf{u}_h) + \mathbf{u}_h\cdot\nabla\mathbf{u}_h\big]\cdot\mathbf{u}_h\,\mathrm{d}\mathbf{x} - \nu\int_\Omega \nabla\mathbf{u}_h : \nabla\mathbf{u}_h\,\mathrm{d}\mathbf{x}\\ &= -\nu\int_\Omega \nabla\mathbf{u}_h : \nabla\mathbf{u}_h\,\mathrm{d}\mathbf{x}\end{aligned}$$

for the total kinetic energy. This proves the global energy stability property $\frac{\mathrm{d}}{\mathrm{d}t}\int_\Omega \eta(\mathbf{u}_h)\,\mathrm{d}\mathbf{x} \le 0$.

2.2. Energy and pressure stabilization

To construct a finite element discretization that satisfies a discrete version of (3), we define

$$m_i = \int_\Omega \varphi_i\,\mathrm{d}\mathbf{x} = \sum_{j=1}^{N_h} m_{ij}, \qquad \tilde{a}_{ij} = \frac{\mathbf{u}_j + \mathbf{u}_i}{2}\cdot\mathbf{c}_{ij} = -\tilde{a}_{ji} \tag{12}$$

and notice that

$$\sum_{j=1}^{N_h}\tilde{a}_{ij} = \frac{1}{2}\int_\Omega \varphi_i(\nabla\cdot\mathbf{u}_h)\,\mathrm{d}\mathbf{x} = -\frac{1}{2}\int_\Omega \mathbf{u}_h\cdot\nabla\varphi_i\,\mathrm{d}\mathbf{x} = \sum_{j=1}^{N_h} a_{ij} \tag{13}$$

under the assumption of periodicity, under which integration by parts produces no boundary terms.

We modify (7) by using the approximations $m_{ij} \approx \tilde{m}_{ij} := m_i\delta_{ij}$ and $a_{ij} \approx \tilde{a}_{ij}$. For stabilization purposes, we use graph Laplacian operators $D^u = (d^u_{ij})_{i,j=1}^{N_h}$ and $D^p = (d^p_{kj})_{k,j=1}^{N_h}$ such that [17]

$$\sum_{j=1}^{N_h} d^u_{ij} = 0, \qquad d^u_{ij} = d^u_{ji} \ge 0 \qquad \forall j \neq i \in \{1,\dots,N_h\}, \tag{14a}$$

$$\sum_{j=1}^{N_h} d^p_{ij} = 0, \qquad d^p_{ij} = d^p_{ji} \ge 0 \qquad \forall j \neq i \in \{1,\dots,N_h\}. \tag{14b}$$

Our stabilized version of the standard Galerkin discretization (7) reads (cf. [50])

$$m_i\frac{\mathrm{d}\mathbf{u}_i}{\mathrm{d}t} = \sum_{j\in\mathcal{N}_i}[(d^u_{ij} - \tilde{a}_{ij} - \nu s_{ij})\mathbf{u}_j - \mathbf{c}_{ij}p_j], \qquad i = 1,\dots,N_h, \tag{15a}$$

$$0 = \sum_{j\in\mathcal{N}_k}[d^p_{kj}p_j - \mathbf{c}_{kj}\cdot\mathbf{u}_j], \qquad k = 1,\dots,N_h. \tag{15b}$$

An operator form of (15), which is better suited for numerical analysis, is presented in (32) below.

Remark 3. The momentum conservation error caused by our modification of (7) is zero because

$$\sum_{i=1}^{N_h}\sum_{j=1}^{N_h}(a_{ij}-\tilde{a}_{ij}+d^u_{ij})\mathbf{u}_j = \sum_{i=1}^{N_h}\sum_{j=1}^{N_h}(a_{ij}-\tilde{a}_{ij})\mathbf{u}_j = \sum_{i=1}^{N_h}\sum_{j=1}^{N_h}(a_{ij}-\tilde{a}_{ij})(\mathbf{u}_j+\mathbf{u}_i) = 0. \tag{16}$$

This follows from (13),(14a), and the fact that $a_{ij} - \tilde{a}_{ij} = -(a_{ji} - \tilde{a}_{ji})$ by definition.

By default, we use $d^u_{ij} = 0$ and the algebraic Becker–Hansbo pressure stabilization ([51], cf. [61])

$$d^p_{ij} = \begin{cases} \omega m_{ij} & \text{if } j \neq i,\\ -\sum_{k\in\mathcal{N}_i\setminus\{i\}} d^p_{ik} & \text{if } j = i\end{cases} \tag{17}$$

depending on a parameter $\omega > 0$. This definition of d^p_{ij} provides the properties required in (14b).

Remark 4. The accuracy of (15) can be improved using the framework of algebraic flux correction to adjust the perturbation of (7) subject to appropriate constraints (see [1,17,62] for details).

2.3. Crank–Nicolson time discretization

We discretize the nonlinear system (15) in time using the semi-implicit Crank–Nicolson method, which is non-dissipative and second-order accurate. In the two-dimensional ($d = 2$) case, we store the components of $\mathbf{u}_i = (u_i, v_i)^\top$ in global vectors $\mathrm{u} = (u_i)_{i=1}^{N_h}$ and $\mathrm{v} = (v_i)_{i=1}^{N_h}$. The pressure unknowns p_k are stored in a global vector $\mathrm{p} = (p_k)_{k=1}^{N_h}$. We denote by $M_L = (m_i\delta_{ij})_{i,j=1}^{N_h}$ the lumped counterpart of the consistent mass matrix $M_C = (m_{ij})_{i,j=1}^{N_h}$. The components of $\mathbf{c}_{ij} = (c^1_{ij}, c^2_{ij})^\top$ are stored in the blocks $C_k = (c^k_{ij})_{i,j=1}^{N_h}$, $k = 1,2$ of a discrete gradient operator. The velocity-dependent coefficients

$$r_{ij}(\mathrm{u},\mathrm{v}) = d^u_{ij}(\mathrm{u},\mathrm{v}) - \tilde{a}_{ij}(\mathrm{u},\mathrm{v}) - \nu s_{ij}$$

are stored in the matrix $R(\mathrm{u},\mathrm{v}) = (r_{ij}(\mathrm{u},\mathrm{v}))_{i,j=1}^{N_h}$, which we update at the beginning of each time step.

To advance the nodal values of numerical approximations $\mathbf{u}_h^n \approx \mathbf{u}_h(\cdot,t^n)$ and $p_h^n \approx p_h(\cdot,t^n)$ in time from a level $t^n = n\Delta t$, $n \in \mathbb{N}_0$ to the level t^{n+1}, we solve the linearized system

$$\begin{bmatrix} M_L - \frac{\Delta t}{2}R(\mathrm{u}^n,\mathrm{v}^n) & 0 & \Delta t C_1\\ 0 & M_L - \frac{\Delta t}{2}R(\mathrm{u}^n,\mathrm{v}^n) & \Delta t C_2\\ \Delta t C_1^\top & \Delta t C_2^\top & \Delta t D^p\end{bmatrix}\begin{bmatrix}\mathrm{u}^{n+1}\\ \mathrm{v}^{n+1}\\ \mathrm{p}^{n+1}\end{bmatrix} = \begin{bmatrix}[M_L + \frac{\Delta t}{2}R(\mathrm{u}^n,\mathrm{v}^n)]\mathrm{u}^n\\ [M_L + \frac{\Delta t}{2}R(\mathrm{u}^n,\mathrm{v}^n)]\mathrm{v}^n\\ 0\end{bmatrix}.$$

To enforce the zero mean condition for p in the periodic case, we modify the last row of the system matrix accordingly. Other types of boundary conditions are handled as in Elman et al. [59, Sec. 3.3].

3. Analysis of stability and consistency

The structure of the spatial semi-discretization (15) is similar to that of algebraic flux correction schemes for the shallow water equations with topography [50] and the compressible Euler equations [35]. Exploiting this similarity, we now extend the analysis in [35, Sect. 3,4] to the incompressible case.

3.1. Energy stability

In our analysis of (15), the kinetic energy $\eta(\mathbf{u}) = \frac{|\mathbf{u}|^2}{2}$ and the flux $\mathbf{q}(\mathbf{u},p) = (\eta(\mathbf{u})+p)\mathbf{u}$ replace entropy pairs $\{\eta,\mathbf{q}\}$ that are used in [35,50] for hyperbolic problems. In the following theorem, we show that the modified finite element discretization (15) of the Navier–Stokes system (1) is *locally energy stable*, i.e., consistent with a semi-discrete version of the energy inequality (3).

Theorem 1. *Assume that the boundary conditions are periodic and*

$$d^u_{ij} - \nu s_{ij} \ge 0, \quad d^p_{ij} \ge 0 \qquad \forall j \neq i \in \{1,\dots,N_h\}. \tag{18}$$

Then a solution to (15) satisfies

$$m_i\frac{\mathrm{d}\eta(\mathbf{u}_i)}{\mathrm{d}t} + \sum_{j\in\mathcal{N}_i\setminus\{i\}} 2|\mathbf{c}_{ij}|\mathcal{Q}(\mathbf{u}_i,p_i,\mathbf{u}_j,p_j;\mathbf{n}_{ij}) \le 0, \tag{19}$$

where $\mathbf{n}_{ij} = \frac{\mathbf{c}_{ij}}{|\mathbf{c}_{ij}|}$ *and* $\mathcal{Q}(\mathbf{u}_L,p_L,\mathbf{u}_R,p_R;\mathbf{n})$ *is a numerical flux consistent with* $\mathbf{q}(\mathbf{u},p)\cdot\mathbf{n}$.

Proof. In view of the row sum properties (11), our semi-discrete scheme (15) can be written as

$$m_i \frac{\mathrm{d}\mathbf{u}_i}{\mathrm{d}t} = \sum_{j\in\mathcal{N}_i\setminus\{i\}} [(d_{ij}^u - \tilde{a}_{ij} - \nu s_{ij})(\mathbf{u}_j - \mathbf{u}_i) - \mathbf{c}_{ij}(p_j - p_i)] - \mathbf{u}_i \sum_{j=1}^{N} \tilde{a}_{ij}, \tag{20a}$$

$$0 = \sum_{j\in\mathcal{N}_i\setminus\{i\}} [d_{ij}^p (p_j - p_i) - (\mathbf{u}_j + \mathbf{u}_i)\cdot \mathbf{c}_{ij}]. \tag{20b}$$

Recalling the definition of $\tilde{a}_{ij}$ and using (20b), we obtain

$$\sum_{j=1}^{N} \tilde{a}_{ij} = \sum_{j\in\mathcal{N}_i\setminus\{i\}} \tilde{a}_{ij} = \sum_{j\in\mathcal{N}_i\setminus\{i\}} \frac{\mathbf{u}_j + \mathbf{u}_i}{2}\cdot\mathbf{c}_{ij} = \sum_{j\in\mathcal{N}_i\setminus\{i\}} \frac{d_{ij}^p}{2}(p_j - p_i). \tag{21}$$

By the chain rule, we have $\frac{\mathrm{d}\eta(\mathbf{u}_i)}{\mathrm{d}t} = \mathbf{u}_i \cdot \frac{\mathrm{d}\mathbf{u}_i}{\mathrm{d}t}$, where $\frac{\mathrm{d}\mathbf{u}_i}{\mathrm{d}t}$ is the time derivative given by (20a). The substitution of (21) and addition of (20b) multiplied by $\frac{|\mathbf{u}_i|^2}{2} + p_i$ yield the evolution equation

$$\begin{aligned} m_i \frac{\mathrm{d}\eta(\mathbf{u}_i)}{\mathrm{d}t} = \mathbf{u}_i \cdot \sum_{j\in\mathcal{N}_i\setminus\{i\}} \left[(d_{ij}^u - \tilde{a}_{ij} - \nu s_{ij})(\mathbf{u}_j - \mathbf{u}_i) - \left(\frac{d_{ij}^p \mathbf{u}_i}{2} + \mathbf{c}_{ij}\right)(p_j - p_i)\right] \\ + \left(\frac{|\mathbf{u}_i|^2}{2} + p_i\right) \sum_{j\in\mathcal{N}_i\setminus\{i\}} [d_{ij}^p (p_j - p_i) - (\mathbf{u}_j + \mathbf{u}_i)\cdot\mathbf{c}_{ij}]. \end{aligned} \tag{22}$$

Following the analysis of entropy-stable schemes for nonlinear hyperbolic problems [1,16,35,50], we use the decomposition $\mathbf{u}_i = \frac{1}{2}(\mathbf{u}_j + \mathbf{u}_i) - \frac{1}{2}(\mathbf{u}_j - \mathbf{u}_i)$ to show that (22) is equivalent to

$$m_i \frac{\mathrm{d}\eta(\mathbf{u}_i)}{\mathrm{d}t} = \sum_{j\in\mathcal{N}_i\setminus\{i\}} [F_{ij} + G_{ij}], \tag{23}$$

where we put all skew-symmetric terms into

$$\begin{aligned} F_{ij} &= \frac{\mathbf{u}_j - \mathbf{u}_i}{2}\cdot\left[\tilde{a}_{ij}(\mathbf{u}_j - \mathbf{u}_i) + \mathbf{c}_{ij}(p_j - p_i)\right] \\ &\quad + (d_{ij}^u - \nu s_{ij})\left(\frac{|\mathbf{u}_j|^2}{2} - \frac{|\mathbf{u}_i|^2}{2}\right) - \frac{d_{ij}^p}{2}\left(\frac{|\mathbf{u}_j|^2}{2} + \frac{|\mathbf{u}_i|^2}{2}\right)(p_j - p_i) \\ &\quad + \frac{1}{2}\left(\frac{|\mathbf{u}_j|^2}{2} + p_j + \frac{|\mathbf{u}_i|^2}{2} + p_i\right)\left[d_{ij}^p(p_j - p_i) - (\mathbf{u}_j + \mathbf{u}_i)\cdot\mathbf{c}_{ij}\right] \\ &= \frac{\tilde{a}_{ij}}{2}|\mathbf{u}_j - \mathbf{u}_i|^2 + \frac{\mathbf{c}_{ij}}{2}\cdot(\mathbf{u}_j - \mathbf{u}_i)(p_j - p_i) \\ &\quad - \frac{\mathbf{u}_j + \mathbf{u}_i}{2}\cdot\mathbf{c}_{ij}\left(\frac{|\mathbf{u}_j|^2}{2} + p_j + \frac{|\mathbf{u}_i|^2}{2} + p_i\right) \\ &\quad + (d_{ij}^u - \nu s_{ij})\left(\frac{|\mathbf{u}_j|^2}{2} - \frac{|\mathbf{u}_i|^2}{2}\right) + d_{ij}^p\left(\frac{p_j^2}{2} - \frac{p_i^2}{2}\right) = -F_{ji} \end{aligned}$$

and all symmetric ones into

$$\begin{aligned} G_{ij} &= -\frac{\mathbf{u}_j + \mathbf{u}_i}{2}\cdot\left[\tilde{a}_{ij}(\mathbf{u}_j - \mathbf{u}_i) + \mathbf{c}_{ij}(p_j - p_i)\right] \\ &\quad - (d_{ij}^u - \nu s_{ij})\frac{|\mathbf{u}_j - \mathbf{u}_i|^2}{2} + \frac{d_{ij}^p}{2}\left(\frac{|\mathbf{u}_j|^2}{2} - \frac{|\mathbf{u}_i|^2}{2}\right)(p_j - p_i) \\ &\quad - \frac{1}{2}\left(\frac{|\mathbf{u}_j|^2}{2} + p_j - \frac{|\mathbf{u}_i|^2}{2} - p_i\right)\left[d_{ij}^p(p_j - p_i) - (\mathbf{u}_j + \mathbf{u}_i)\cdot\mathbf{c}_{ij}\right] \\ &= \left(\frac{\mathbf{u}_j + \mathbf{u}_i}{2}\cdot\mathbf{c}_{ij} - \tilde{a}_{ij}\right)\left(\frac{|\mathbf{u}_j|^2}{2} - \frac{|\mathbf{u}_i|^2}{2}\right) \\ &\quad - (d_{ij}^u - \nu s_{ij})\frac{|\mathbf{u}_j - \mathbf{u}_i|^2}{2} - d_{ij}^p\frac{(p_j - p_i)^2}{2} \\ &= -(d_{ij}^u - \nu s_{ij})\frac{|\mathbf{u}_j - \mathbf{u}_i|^2}{2} - d_{ij}^p\frac{(p_j - p_i)^2}{2} = G_{ji}. \end{aligned}$$

The fluxes $F_{ij} = -F_{ji}$ have no influence on the total kinetic energy $\sum_{i=1}^{N_h} m_i\eta(\mathbf{u}_i) \approx \int_\Omega \eta(\mathbf{u})\,\mathrm{d}\mathbf{x}$ because they cancel out upon summation of (23) over i. The local energy inequality (19) with

$$\mathcal{Q}(\mathbf{u}_i, p_i, \mathbf{u}_j, p_j; \mathbf{n}_{ij}) = -\frac{F_{ij}}{2|\mathbf{c}_{ij}|}$$

follows from (23) since $G_{ij} \le 0$ by (18). The consistency requirement is met because $\mathcal{Q}(\mathbf{u}_i, p_i, \mathbf{u}_j, p_j; \mathbf{n}_{ij})$ reduces to $\mathbf{q}(\mathbf{u}, p)\cdot\mathbf{n}_{ij}$ for $\mathbf{u}_i = \mathbf{u} = \mathbf{u}_j$, $p_i = p = p_j$. The proof of the theorem is complete. □

Remark 5. In view of the fact that lumped-mass $\mathbb{P}_1$ finite element approximations are equivalent to vertex-centered finite volume schemes [63,64], the weight $2|\mathbf{c}_{ij}|$ of the semi-discrete inequality (19) corresponds to the surface area associated with the numerical energy flux $\mathcal{Q}(\mathbf{u}_i, p_i, \mathbf{u}_j, p_j; \mathbf{n}_{ij})$.

Remark 6. Proving energy stability for mixed finite element pairs (such as Taylor–Hood elements) is more difficult because we cannot multiply (20b) by $|\mathbf{u}_i|^2/2 + p_i$ to derive F_{ij} and G_{ij} as above.

The next lemma adapts the 'weak BV estimate' obtained in [35, Lem. 1] to incompressible flows.

Lemma 1. *For any finite time $T > 0$, a solution of the semi-discrete problem (20) satisfies*

$$\int_0^T \sum_{i=1}^{N_h} \sum_{j\in\mathcal{N}_i\setminus\{i\}} \left[\frac{d_{ij}^{\mathrm{add}}}{2}|\mathbf{u}_j - \mathbf{u}_i|^2 + \frac{d_{ij}^p}{2}(p_j - p_i)^2\right] \mathrm{d}t = C_T, \tag{24}$$

where $d_{ij}^{\mathrm{add}} = d_{ij}^u - \nu s_{ij}$ and $C_T = \sum_{i=1}^{N_h} m_i\eta(\mathbf{u}_i(0)) - \sum_{i=1}^{N_h} m_i\eta(\mathbf{u}_i(T))$.

Proof. Using (23) and the property that $F_{ij} = -F_{ji}$, we find that

$$\sum_{i=1}^{N_h} m_i \frac{\mathrm{d}\eta(\mathbf{u}_i)}{\mathrm{d}t} = \sum_{i=1}^{N_h} \sum_{j\in\mathcal{N}_i\setminus\{i\}} G_{ij}, \tag{25}$$

where

$$G_{ij} = -\frac{d_{ij}^{\mathrm{add}}}{2}|\mathbf{u}_j - \mathbf{u}_i|^2 - \frac{d_{ij}^p}{2}(p_j - p_i)^2.$$

Integrating (25) from $t = 0$ to $t = T$, we obtain (24). □

The importance of Lemma 1 lies in the fact that (24) provides a weak bound for the derivatives of the velocity and pressure approximations. Specifically, we have the following auxiliary result, cf. [35].

Lemma 2. *Under the assumption that the sequence of meshes $\{\mathcal{T}_h\}_{h\searrow 0}$ is shape regular and quasi-uniform, there exist constants $C_1, C_2 > 0$ independent of h such that*

$$C_1 h|v_h|_{H^1(\Omega)}^2 \le \sum_{i=1}^{N_h} \sum_{j\in\mathcal{N}_i\setminus\{i\}} h^{d-1}|v_j - v_i|^2 \le C_2 h|v_h|_{H^1(\Omega)}^2 \qquad \forall v_h \in V_h.$$

Proof. The proof that we present below was originally obtained in [35, Lem. 2] using an auxiliary result from [65, Lem. 2.2].

Let $\mathcal{N}_K$ contain the indices of nodes belonging to an element $K \in \mathcal{T}_h$. Denote the local mesh size by h_K. Construct $b_h(v_h, v_h) = \sum_{K\in\mathcal{T}_h} b_K(v_h, v_h)$ using the local bilinear forms

$$b_K(v_h, w_h) = h_K^{d-1} \sum_{i\in\mathcal{N}_K} \sum_{j\in\mathcal{N}_K\setminus\{i\}} (v_j - v_i)^{\mathrm{T}}(w_j - w_i).$$

Guermond and Popov [65, Lemma 2.2] showed that

$$c_1|v_h|_{H^1(K)}^2 \le \frac{h_K^{1-d}\|J_K^{-1}\|^2}{|\det J_K^{-1}|} b_K(v_h, v_h) \le c_2|v_h|_{H^1(K)}^2,$$

where J_K is the Jacobian of the affine mapping from the reference element $\hat{K}$ to K. The derivation of the above estimates exploits the equivalence of all norms for polynomials defined on $\hat{K}$. The powers of h_K are due to the change of variables. The assertion of the lemma follows from the fact that $|\det J_K^{-1}| = \mathcal{O}(h_K^{-d})$ and $\|J_K^{-1}\| = \mathcal{O}(h_K^{-1})$ under the assumption of shape regularity. □

3.2. Lax–Wendroff consistency

The use of row-sum mass lumping on the left-hand side of (15a) is equivalent to approximating the $L^2(\Omega)$ scalar product $\int_\Omega \frac{\partial \mathbf{u}_h}{\partial t} \cdot \mathbf{v}_h \, \mathrm{d}\mathbf{x} = (\frac{\partial \mathbf{u}_h}{\partial t}, \mathbf{v}_h)_{L^2(\Omega)}$ of the Galerkin weak form (6) by [1, Ch. 8]

$$\left(\frac{\partial \mathbf{u}_h}{\partial t}, \mathbf{v}_h\right)_{L_h^2(\Omega)} = \sum_{i=1}^{N_h} m_i \mathbf{v}_i \cdot \frac{\mathrm{d}\mathbf{u}_i}{\mathrm{d}t}. \tag{26}$$

The discretized momentum Eq. (6a) also contains the nonlinear term

$$\begin{aligned} a(\mathbf{u}_h, \mathbf{v}_h) &= \frac{1}{2}\int_\Omega [\nabla \cdot (\mathbf{u}_h \otimes \mathbf{u}_h) + \mathbf{u}_h \cdot \nabla \mathbf{u}_h] \cdot \mathbf{v}_h \, \mathrm{d}\mathbf{x} + \nu \int_\Omega \nabla \mathbf{u}_h : \nabla \mathbf{v}_h \, \mathrm{d}\mathbf{x} \\ &= \sum_{i=1}^{N_h} \mathbf{v}_i \cdot \sum_{j \in \mathcal{N}_i} (a_{ij} + \nu s_{ij}) \mathbf{u}_j \\ &= -\sum_{i=1}^{N_h} \sum_{j=i+1}^{N_h} a_{ij} (\mathbf{u}_j \cdot \mathbf{v}_i - \mathbf{u}_i \cdot \mathbf{v}_j) \\ &\quad - \sum_{i=1}^{N_h} \sum_{j=i+1}^{N_h} \nu s_{ij} (\mathbf{u}_j - \mathbf{u}_i) \cdot (\mathbf{v}_j - \mathbf{v}_i). \end{aligned} \tag{27}$$

In our semi-discrete scheme (15), we stabilize $a(\mathbf{u}_h, \mathbf{v}_h)$ by subtracting

$$\begin{aligned} s_h^u(\mathbf{u}_h, \mathbf{v}_h) &= \sum_{i=1}^{N_h} \mathbf{v}_i \cdot \sum_{j \in \mathcal{N}_i} (a_{ij} - \tilde{a}_{ij} + d_{ij}^u) \mathbf{u}_j \\ &= -\sum_{i=1}^{N_h} \sum_{j=i+1}^{N_h} (a_{ij} - \tilde{a}_{ij}) (\mathbf{u}_j + \mathbf{u}_i) \cdot (\mathbf{v}_j - \mathbf{v}_i) \\ &\quad - \sum_{i=1}^{N_h} \sum_{j=i+1}^{N_h} d_{ij}^u (\mathbf{u}_j - \mathbf{u}_i) \cdot (\mathbf{v}_j - \mathbf{v}_i). \end{aligned} \tag{28}$$

Here, we used the conservation property (16) to derive the second identity. The linear term

$$\begin{aligned} b(\mathbf{v}_h, p_h) &= \int_\Omega \nabla p_h \cdot \mathbf{v}_h \, \mathrm{d}\mathbf{x} = \sum_{i=1}^{N_h} \mathbf{v}_i \cdot \sum_{j \in \mathcal{N}_i} \mathbf{c}_{ij} p_j = \sum_{i=1}^{N_h} \mathbf{v}_i \cdot \sum_{j=1}^{N_h} \mathbf{c}_{ij} (p_j + p_i) \\ &= \sum_{i=1}^{N_h} \sum_{j=i+1}^{N_h} \mathbf{c}_{ij} \cdot (\mathbf{v}_i - \mathbf{v}_j)(p_j + p_i) \end{aligned} \tag{29}$$

of the Galerkin momentum equation remains unchanged. The pressure is stabilized using

$$s_h^p(p_h, q_h) = \sum_{i=1}^{N_h} q_i \sum_{j \in \mathcal{N}_i \setminus \{i\}} d_{ij}^p (p_j - p_i) = -\sum_{i=1}^{N_h} \sum_{j=i+1}^{N_h} d_{ij}^p (p_j - p_i)(q_j - q_i). \tag{30}$$

Substituting the Becker–Hansbo definition (17) of d_{ij}^p into (30), we obtain

$$s_h^p(p_h, q_h) = \omega[(p_h, q_h)_{L^2(\Omega)} - (p_h, q_h)_{L_h^2(\Omega)}] = -\omega \sum_{i=1}^{N_h} \sum_{j=i+1}^{N_h} m_{ij} (p_j - p_i)(q_j - q_i). \tag{31}$$

The semi-discrete problem associated with (15) can now be written in the generic operator form

$$\left(\frac{\partial \mathbf{u}_h}{\partial t}, \mathbf{v}_h\right)_{L_h^2(\Omega)} + a(\mathbf{u}_h, \mathbf{v}_h) + b(\mathbf{v}_h, p_h) = s_h^u(\mathbf{u}_h, \mathbf{v}_h) \qquad \forall \mathbf{v}_h \in \mathbf{V}_h, \tag{32a}$$

$$b(\mathbf{u}_h, q_h) = s_h^p(p_h, q_h) \qquad \forall q_h \in V_h. \tag{32b}$$

The standard finite element interpolation operator $I_h : C(\bar{\Omega}) \to V_h$ approximates $v \in C(\bar{\Omega})$ by a piecewise-linear function $I_h v = \sum_{i=1}^{N_h} v_i \varphi_i \in V_h$ such that $v_i = v(\mathbf{x}_i)$ (see, e.g., [66]). We say that the stabilization built into the semi-discrete scheme (32) is *Lax–Wendroff consistent* if

$$s_h^u(\mathbf{u}_h, \mathbf{v}_h) \to 0, \qquad s_h^p(p_h, q_h) \to 0 \qquad \text{as } h \to 0$$

for finite element interpolants $\mathbf{v}_h = I_h \mathbf{v} \in \mathbf{V}_h$ and $q_h = I_h q \in V_h$ of smooth test functions $\mathbf{v}$ and q.

Lemma 3. *Assume that $\|p_h\|_{L^2(\Omega)}$ is bounded by a constant independent of h. Then the pressure stabilization term $s_h^p(p_h, q_h)$ defined by (31) is Lax–Wendroff consistent.*

Proof. Following the proofs of [1, Lem. 8.72] and [1, Cor. 8.74], we define

$$e_h(q_h) = \sup_{p_h \in V_h} \frac{|(p_h, q_h)_{L^2(\Omega)} - (p_h, q_h)_{L_h^2(\Omega)}|}{\|p_h\|_{L^2(\Omega)}} \qquad \forall q_h \in V_h$$

as the consistency error of Strang's first lemma applied to lumped L^2 projections. As shown in [1, Lem. 8.54 + Cor. 8.74] using the result obtained in [67, Lem. 1] and interpolation error estimates, there is a constant $C > 0$ independent of h such that

$$e_h(q_h) \le Ch|q_h|_{H^1(\Omega)}.$$

Since $|s_h^p(p_h, q_h)| \le \omega \|p_h\|_{L^2(\Omega)} e_h(q_h)$, it follows that

$$|s_h^p(p_h, q_h)| \le C\omega h \|p_h\|_{L^2(\Omega)} |q_h|_{H^1(\Omega)},$$

where $\|p_h\|_{L^2(\Omega)}$ is bounded by assumption and $|q_h|_{H^1(\Omega)} = |I_h q|_{H^1(\Omega)} \le C\|q\|_{H^2(\Omega)}$. This estimate of the error due to mass lumping proves the Lax–Wendroff consistency of $s_h^p(p_h, q_h)$. □

Adapting the flux correction schemes presented in [1,17,35] to the incompressible case, we define

$$d_{ij}^u = \begin{cases} (1 - \alpha_{ij}) d_{ij}^{\max} & \text{if } j \neq i, \\ -\sum_{k \in \mathcal{N}_i \setminus \{i\}} d_{kj}^u & \text{if } j = i, \end{cases} \tag{33}$$

where $\alpha_{ij} \in [0, 1]$ is an appropriately chosen correction factor and

$$d_{ij}^{\max} = \begin{cases} |a_{ij}| & \text{if } j \neq i, \\ -\sum_{k \in \mathcal{N}_i \setminus \{i\}} d_{kj}^{\max} & \text{if } j = i \end{cases} \tag{34}$$

is the artificial viscosity coefficient of the low-order *discrete upwinding* [17] method. Let

$$d_h(\mathbf{u}_h, \mathbf{v}_h) = \sum_{i=1}^{N_h} \sum_{j=i+1}^{N_h} d_{ij}^u (\mathbf{u}_j - \mathbf{u}_i) \cdot (\mathbf{v}_j - \mathbf{v}_i). \tag{35}$$

Then for $d_{ij}^{\max} = \mathcal{O}(h^{d-1})$ and any choice of $\alpha_{ij} \in [0, 1]$, we have the estimate [62]

$$|d_h(\mathbf{u}_h, \mathbf{v}_h)| \le \sqrt{d_h(\mathbf{u}_h, \mathbf{u}_h)} \sqrt{d_h(\mathbf{v}_h, \mathbf{v}_h)} \le Ch |\mathbf{u}_h|_{H^1(\Omega)} |\mathbf{v}_h|_{H^1(\Omega)}. \tag{36}$$

If Lemmas 1 and 2 are applicable, then $h^{\frac{1}{2}} |\mathbf{u}_h|_{H^1(\Omega)}$ is bounded and

$$|d_h(\mathbf{u}_h, \mathbf{v}_h)| \le Ch^{\frac{1}{2}} |\mathbf{v}_h|_{H^1(\Omega)} = Ch^{\frac{1}{2}} |I_h \mathbf{v}|_{H^1(\Omega)} \le Ch^{\frac{1}{2}} \|\mathbf{v}\|_{H^2(\Omega)}.$$

We use this estimate of the consistency error in the proof of the following lemma.

Lemma 4.

The velocity stabilization term $s_h^u(\mathbf{u}_h, \mathbf{v}_h)$ defined by (28) with $d_{ij}^{\max} = \mathcal{O}(h^{d-1})$ is Lax–Wendroff consistent under the assumptions of Lemmas 1 and 2.

Proof. The stabilization term (28) of the momentum Eq. (32a) admits the decomposition

$$s_h^u(\mathbf{u}_h, \mathbf{v}_h) = \sum_{i=1}^{N_h} \mathbf{v}_i \cdot \sum_{j=i}^{N_h} (a_{ij} - \tilde{a}_{ij}) \mathbf{u}_j - d_h(\mathbf{u}_h, \mathbf{v}_h),$$

where

$$\begin{aligned} a_{ij} - \tilde{a}_{ij} &= \frac{1}{2} \int_\Omega [\varphi_i \mathbf{u}_h \cdot \nabla \varphi_j - \varphi_j \mathbf{u}_h \cdot \nabla \varphi_i] \, \mathrm{d}\mathbf{x} - \frac{\mathbf{u}_j + \mathbf{u}_i}{2} \cdot \int_\Omega \varphi_i \nabla \varphi_j \, \mathrm{d}\mathbf{x} \\ &= \frac{1}{2} \int_\Omega [\varphi_i (\mathbf{u}_h - \mathbf{u}_i) \cdot \nabla \varphi_j - \varphi_j (\mathbf{u}_h - \mathbf{u}_j) \cdot \nabla \varphi_i] \, \mathrm{d}\mathbf{x} \end{aligned}$$

and therefore

$$\begin{aligned} s_h^u(\mathbf{u}_h,\mathbf{v}_h) =& \frac{1}{2}\int_\Omega (\mathbf{v}_h\otimes\mathbf{u}_h - I_h(\mathbf{v}_h\otimes\mathbf{u}_h)) : \nabla\mathbf{u}_h \,\mathrm{d}\mathbf{x} \\ &-\frac{1}{2}\int_\Omega [\mathbf{u}_h\otimes\mathbf{u}_h - I_h(\mathbf{u}_h\otimes\mathbf{u}_h)] : \nabla\mathbf{v}_h \,\mathrm{d}\mathbf{x} - d_h(\mathbf{u}_h,\mathbf{v}_h), \\ =& \frac{1}{2}\sum_{e=1}^{E_h} \nabla\mathbf{u}_h|_{K^e} : \left[\int_{K^e} (\mathbf{v}_h\otimes\mathbf{u}_h - I_h(\mathbf{v}_h\otimes\mathbf{u}_h))\,\mathrm{d}\mathbf{x}\right] \\ &-\frac{1}{2}\sum_{e=1}^{E_h} \nabla\mathbf{v}_h|_{K^e} : \left[\int_{K^e} [\mathbf{u}_h\otimes\mathbf{u}_h - I_h(\mathbf{u}_h\otimes\mathbf{u}_h)]\,\mathrm{d}\mathbf{x}\right] - d_h(\mathbf{u}_h,\mathbf{v}_h). \end{aligned}$$

For scalar linear polynomials $u_h, v_h \in \mathbb{P}_1(K^e)$, we can show that

$$\begin{aligned} \left|\int_{K^e} (v_h u_h - I_h(v_h u_h))\,\mathrm{d}\mathbf{x}\right| &= |(v_h,u_h)_{L^2(K^e)} - (v_h,u_h)_{L_h^2(K^e)}| \\ &\le Ch\|u_h\|_{L^2(K^e)}|v_h|_{H^1(K^e)} \end{aligned}$$

as in Lemma 3. This enables us to estimate individual contributions of $K \in \mathcal{T}_h$ to $s_h^u(\mathbf{u}_h,\mathbf{v}_h)$. To complete the proof, we exploit the boundedness of $|\mathbf{v}_h|_{H^1(\Omega)} = |I_h\mathbf{v}|_{H^1(\Omega)} \le C\|\mathbf{v}\|_{H^2(\Omega)}$ for smooth $\mathbf{v}$, and (similarly to [35, Thm. 3]) the weak BV bound for $h^{\frac{1}{2}}|\mathbf{u}_h|_{H^1(\Omega)}$ provided by Lemmas 1 and 2. □

Lemma 5. *The Galerkin part of the scheme (32) is Lax–Wendroff consistent in the sense that*

$$b(\mathbf{v}_h,p_h) = -\int_\Omega p_h(\nabla\cdot\mathbf{v}_h)\,\mathrm{d}\mathbf{x}, \qquad b(\mathbf{u}_h,q_h) = \int_\Omega \mathbf{u}_h\cdot\nabla q_h\,\mathrm{d}\mathbf{x},$$

$$\left|a(\mathbf{u}_h,\mathbf{v}_h) - \int_\Omega (\nu\nabla\mathbf{u}_h - \mathbf{u}_h\otimes\mathbf{u}_h) : \nabla\mathbf{v}_h\,\mathrm{d}\mathbf{x}\right| \to 0 \qquad \text{as } h\to 0.$$

Proof. In view of the vector identity $\nabla\cdot(\mathbf{u}_h\otimes\mathbf{u}_h) = \mathbf{u}_h\cdot\nabla\mathbf{u}_h + \mathbf{u}_h\nabla\cdot\mathbf{u}_h$, it is sufficient to show that the consistency error $R_h = \int_\Omega(\nabla\cdot\mathbf{u}_h)\mathbf{u}_h\cdot\mathbf{v}_h\,\mathrm{d}\mathbf{x}$ vanishes in the limit $h\to 0$. By (32b), we have

$$\begin{aligned} R_h &= \int_\Omega (\nabla\cdot\mathbf{u}_h) I_h(\mathbf{u}_h\cdot\mathbf{v}_h)\,\mathrm{d}\mathbf{x} + \int_\Omega (\nabla\cdot\mathbf{u}_h)[\mathbf{u}_h\cdot\mathbf{v}_h - I_h(\mathbf{u}_h\cdot\mathbf{v}_h)]\,\mathrm{d}\mathbf{x} \\ &= -s_h^p(p_h, I_h(\mathbf{u}_h\cdot\mathbf{v}_h)) + \sum_{e=1}^{E_h} (\nabla\cdot\mathbf{u}_h)|_{K^e}\left[(\mathbf{u}_h,\mathbf{v}_h)_{L^2(K^e)} - (\mathbf{u}_h,\mathbf{v}_h)_{L_h^2(K^e)}\right]. \end{aligned}$$

To complete the proof, we invoke Lemma 3 and estimate the lumping error as in Lemma 4. □

We are now ready to formulate the main consistency result of this section. In the following theorem, functions belonging to the space $C_c^2(\bar\Omega\times[0,T))$ have compact support in time.

Theorem 2 (*Lax–Wendroff Consistency of the Energy-stable FEM*)**.** *Let $T>0$ be a final time. Assume that Lemmas 1–5 are applicable, and a sequence of approximations $(\mathbf{u}_h,p_h)$ obtained with (32) converges to a limit $(\mathbf{u},p)$ strongly. Then $(\mathbf{u},p)$ is a weak solution of problem (1) in the sense that*

$$\int_0^T\int_\Omega \left[\mathbf{u}\cdot\frac{\partial\mathbf{v}}{\partial t} + (\mathbf{u}\otimes\mathbf{u} - \nu\nabla\mathbf{u}) : \nabla\mathbf{v} + p\nabla\cdot\mathbf{v}\right]\mathrm{d}\mathbf{x}\,\mathrm{d}t + \int_\Omega \mathbf{u}(\mathbf{x},0)\cdot\mathbf{v}(\mathbf{x},0)\,\mathrm{d}\mathbf{x} = 0, \tag{37a}$$

$$\int_\Omega \mathbf{u}\cdot\nabla q = 0 \tag{37b}$$

holds for all test functions $\mathbf{v}\in[C_c^2(\bar\Omega\times[0,T))]^d$ and $q\in C^1(\bar\Omega)$ that are periodic in space.

Proof. Let $\mathbf{v}_h = I_h\mathbf{v}$ and $q_h = I_h q$ for test functions $\mathbf{v}$ and q that meet the assumptions of the theorem. The consistency error due to mass lumping in the time derivative term can be estimated as in [35, Thm. 3]. The Lax–Wendroff consistency of the remaining terms can be shown using Lemmas 1–5. We skip the details here because we present them in the proof of Theorem 3 below. □

4. Convergence analysis

In this section, we adapt the convergence theory developed in [35, Sec. 5] for flux-corrected finite element discretizations of the compressible Euler equations to the incompressible case, i.e., to the vanishing viscosity limit of problem (1). The existence and uniqueness of a classical solution to

$$\begin{aligned} \frac{\partial\mathbf{u}}{\partial t} + \frac{1}{2}[\nabla\cdot(\mathbf{u}\otimes\mathbf{u}) + \mathbf{u}\cdot\nabla\mathbf{u}] + \nabla p = 0 \qquad & \text{in } \Omega\times(0,\infty), \\ \nabla\cdot\mathbf{u} = 0 \qquad & \text{in } \Omega\times(0,\infty), \\ \mathbf{u}(\cdot,0) = \mathbf{u}_0, \qquad \nabla\cdot\mathbf{u}_0 = 0 \qquad & \text{in } \Omega \end{aligned} \tag{38}$$

can be guaranteed under suitable assumptions on the initial conditions [68,69], e.g., for $\mathbf{u}_0\in H^k$. If these assumptions are violated, weak solutions of the incompressible Euler Eqs. (38) may develop singularities, such as blow-ups in vorticity. The framework of classical and weak solutions is insufficient for an adequate mathematical description of turbulent or highly irregular flows. Therefore, the concept of measure-valued solutions was introduced by DiPerna [70] already in the 1980s. Following a more recent trend [53,55,71,72], we analyze *dissipative measure-valued* (DMV) solutions in this article. In situations where the classical solution concept breaks down, DMV solutions provide an alternative that handles energy dissipation, oscillations and concentrations in a physics-compatible manner.

To give a formal definition of dissipative measure-valued solutions to the incompressible Euler system (38), we first introduce the necessary notation. Let $\tilde{\mathbf{u}}$ represent a generic element of the phase space $\mathcal{F}_{\text{inc}} = \mathbb{R}^d$. The space of all probability measures on $\mathcal{F}_{\text{inc}}$ is denoted by $\mathcal{P}(\mathcal{F})$ in what follows. The notation $\mathcal{M}^+(\overline{\Omega})$ is used for the set of all positive *Radon measures* that can be identified with the space of all linear forms on $C_c(\overline{\Omega})$. If $\overline{\Omega}$ is compact, then $[C_c(\overline{\Omega})]^* = \mathcal{M}(\overline{\Omega})$. Furthermore, we denote by $\mathcal{M}(\overline{\Omega},\mathbb{R}^{d\times d}_{\text{sym}})$ the set of symmetric matrix-valued measures and by $\mathcal{M}^+(\overline{\Omega};\mathbb{R}^{d\times d}_{\text{sym}})$ the set of symmetric positive-definite matrix-valued measures, i.e.,

$$\begin{aligned} \mathcal{M}^+(\overline{\Omega},\mathbb{R}^{d\times d}_{\text{sym}}) = \Bigg\{ \nu\in\mathcal{M}(\overline{\Omega},\mathbb{R}^{d\times d}_{\text{sym}}) \Bigg| \int_{\overline{\Omega}} \phi(\xi\otimes\xi) : \mathrm{d}\nu \ge 0 \\ \text{for any } \xi\in\mathbb{R}^d, \phi\in C_c(\overline{\Omega}), \phi\ge 0 \Bigg\}. \end{aligned}$$

We are now ready to list the properties that define a DMV solution in the work of Arun et al. [55].

Definition 1 (*Dissipative Measure-valued Solution*)**.** A family of probability measures

$$\mathcal{U} = \{\mathcal{U}_{\mathbf{x},t}\}_{(\mathbf{x},t)\in\Omega\times(0,T)} \in L^\infty_{\text{weak}-*}(\Omega\times(0,T);\mathcal{P}(\mathcal{F}_{\text{inc}}))$$

is a dissipative measure-valued solution of (38) with initial data $\mathbf{u}_0$ if the following conditions hold:

- **Energy inequality** – The integral inequality
$$\frac{1}{2}\int_\Omega \langle\mathcal{U}_{\mathbf{x},t};|\tilde{\mathbf{u}}|^2\rangle\,\mathrm{d}\mathbf{x} + \int_\Omega \mathrm{d}D_{cd}(t) \le \frac{1}{2}\int_\Omega |\mathbf{u}_0|^2\,\mathrm{d}\mathbf{x} \tag{39}$$
holds for almost every $t\in(0,T)$ with $D_{cd}\in L^\infty(0,T;\mathcal{M}^+(\Omega))$.
- **Divergence-free condition** – The integral identity
$$\int_\Omega \langle\mathcal{U}_{\mathbf{x},t};\tilde{\mathbf{u}}\rangle\cdot\nabla q\,\mathrm{d}\mathbf{x} = 0 \tag{40}$$
holds for almost every $t\in(0,T)$ and for all $q\in C_c^\infty(\Omega)$.
- **Momentum equation** – The integral identity
$$\begin{aligned} &\int_0^T\int_\Omega \left(\langle\mathcal{U}_{\mathbf{x},t};\tilde{\mathbf{u}}\rangle\cdot\partial_t\mathbf{v} + \langle\mathcal{U}_{\mathbf{x},t};\tilde{\mathbf{u}}\otimes\tilde{\mathbf{u}}\rangle : \nabla\mathbf{v}\right)\mathrm{d}\mathbf{x}\,\mathrm{d}t \\ &+ \int_0^T\int_\Omega \nabla\mathbf{v} : \mathrm{d}\mathfrak{M}_{cd}(t)\,\mathrm{d}t + \int_\Omega \mathbf{u}_0\cdot\mathbf{v}(\cdot,0)\,\mathrm{d}\mathbf{x} = 0 \end{aligned} \tag{41}$$
holds for all $\mathbf{v}\in C_c^\infty(\Omega\times[0,T);\mathbb{R}^d)$ with $\nabla\cdot\mathbf{v} = 0$, where $\mathfrak{M}_{cd}\in L^\infty(0,T;\mathcal{M}(\Omega;\mathbb{R}^{d\times d}))$.

- **Defect compatibility condition** – There exists $c > 0$ such that for almost every $t \in (0,T)$

$$|\mathfrak{M}_{cd}(t)|(\Omega) \le cD(t), \tag{42}$$

where $D(t) = \int_\Omega \mathrm{d}D_{cd}(t) > 0 \in L^\infty(0,T)$ denotes the dissipation defect.

Remark 7. A definition of DMV solutions was recently given in [73] for general systems of conservation laws. In particular, it is valid for the compressible and incompressible Euler equations, as well as for the shallow water magnetohydrodynamics equations. Moreover, a weak-strong uniqueness result was obtained in [73]. Focusing on this particular definition, we remark that any DMV solution to the incompressible Euler system is generated by a sequence of energy-admissible weak solutions $\{\mathbf{u}_n\}_{n\in\mathbb{N}}$ of that system [52]. The dissipation defect and the defect in the momentum arise because the weak-$*$ limit of corresponding nonlinear terms does not coincide with the classical limit. We have

$$D_{cd}(t) = \overline{\eta(\mathbf{u})}(t,\cdot) - \frac{1}{2}\langle \mathcal{U}_{\mathbf{x},t}; |\tilde{\mathbf{u}}|^2\rangle, \qquad \mathfrak{M}_{cd}(t) = \overline{\mathbf{u}\otimes\mathbf{u}}(t,\cdot) - \langle \mathcal{U}_{(\mathbf{x},t)}; \tilde{\mathbf{u}}\otimes\tilde{\mathbf{u}}\rangle,$$

where $\overline{\eta(\mathbf{u})}$ is the weak-$*$ limit of $\eta(\mathbf{u}_n) = \frac{1}{2}|\mathbf{u}_n|^2 \in L^\infty(0,T;\mathcal{M}^+(\Omega))$ for $n \in \mathbb{N}$ and $\mathbf{u}\otimes\mathbf{u}$ is the weak-$*$ limit of $\{\mathbf{u}_n \otimes \mathbf{u}_n\}_{n\in\mathbb{N}}$ in $L^\infty(0,T;\mathcal{M}(\Omega;\mathbb{R}^{d\times d}))$. In this context, weak-strong uniqueness implies that the defect measures disappear for a classical solution to the incompressible Euler system, and the probability measure becomes a δ-distribution, as demonstrated in [72].

Following our analysis of flux-corrected finite element discretizations of the compressible Euler equations [35], we now adapt the consistency result established in Theorem 2 as follows.

Theorem 3 (*Consistency in the Vanishing Viscosity Limit*)**.** *Assume that Lemmas 1–5 are applicable on the time interval $[0,T]$ and let the initial data $\mathbf{u}_{h,0}$ be admissible. Denote by $\mathbf{U}_h = (\mathbf{u}_h, p_h)$ a uniformly bounded numerical solution to system (38) obtained with the scheme (32). Define the consistency errors $e_{q_h}(q,t)$ and $e_{\mathbf{u}_h}(\mathbf{v},t)$ w.r.t. test functions q and $\mathbf{v}$, respectively, by the property that*

- *For any $q \in C_c^1(\Omega)$ and a.e. $t \in (0,T)$*

$$\int_\Omega \mathbf{u}_h \cdot \nabla q \,\mathrm{d}\mathbf{x} = e_{q_h}(q,t). \tag{43}$$

- *For any $\mathbf{v} \in C_c^2([0,T)\times\Omega;\mathbb{R}^d)$ with $\nabla\cdot\mathbf{v} = 0$ and any $\tau \in (0,T]$*

$$\left[\int_\Omega \mathbf{u}_h\cdot\mathbf{v}\,\mathrm{d}\mathbf{x}\right]_{t=0}^{t=\tau} = \int_0^\tau\int_\Omega \left[\mathbf{u}_h\cdot\frac{\partial\mathbf{v}}{\partial t} + (\mathbf{u}_h\otimes\mathbf{u}_h) : \nabla\mathbf{v}\right]\mathrm{d}\mathbf{x}\,\mathrm{d}t + \int_0^\tau e_{\mathbf{u}_h}(\mathbf{v},t)\,\mathrm{d}t. \tag{44}$$

Then the semi-discrete scheme (32) is consistent with the weak form of the incompressible Euler Eqs. (38) in the sense that $\|e_{q_h}\|_{L^1(0,T)} \to 0$ and $\|e_{\mathbf{u}_h}\|_{L^1(0,T)} \to 0$ as $h \to 0$.

Proof. To derive 3 following the proof of Lemma 5, we use the splitting $q = q_h + (q - q_h)$, where $q_h = I_h q$ is the interpolant of the smooth test function q. Using the definition 3 of the consistency error $e_{q_h}(q,t)$ and integration by parts under the assumption of periodicity, we find that

$$e_{q_h}(q,t) = -\int_\Omega q\nabla\cdot\mathbf{u}_h\,\mathrm{d}\mathbf{x} = \int_\Omega \underbrace{(q_h - q)}_{\mathcal{O}(h^2)}(\nabla\cdot\mathbf{u}_h)\,\mathrm{d}\mathbf{x} - \int_\Omega q_h(\nabla\cdot\mathbf{u}_h)\,\mathrm{d}\mathbf{x} \overset{(32b)}{=} \mathcal{O}(h^2) + s_h^p(p_h,q_h).$$

The application of Lemma 3 proves that $e_{q_h}(q,t)$ vanishes in the limit $h \to 0$.

To prove the consistency of (44) with the momentum equation, we first notice that the identity

$$\left[\int_\Omega \mathbf{u}_h\cdot\mathbf{v}\,\mathrm{d}\mathbf{x}\right]_{t=0}^{t=\tau} = \int_0^\tau\int_\Omega \frac{\partial}{\partial t}(\mathbf{u}_h\cdot\mathbf{v})\,\mathrm{d}\mathbf{x}\,\mathrm{d}t = \int_0^\tau\int_\Omega \left[\mathbf{u}_h\cdot\frac{\partial\mathbf{v}}{\partial t} + \frac{\partial\mathbf{u}_h}{\partial t}\cdot\mathbf{v}\right]\mathrm{d}\mathbf{x}\,\mathrm{d}t$$

holds for all $\mathbf{v} \in C_c^2(\Omega\times[0,T);\mathbb{R}^d)$. Using the interpolation error estimate for the difference between the smooth divergence-free test function $\mathbf{v}$ and its interpolant $\mathbf{v}_h = I_h\mathbf{v}$, we find that

$$\int_\Omega \frac{\partial\mathbf{u}_h}{\partial t}\cdot\mathbf{v}\,\mathrm{d}\mathbf{x} = \int_\Omega \frac{\partial\mathbf{u}_h}{\partial t}\cdot\underbrace{(\mathbf{v}-\mathbf{v}_h)}_{\mathcal{O}(h^2)}\,\mathrm{d}\mathbf{x} + \int_\Omega \frac{\partial\mathbf{u}_h}{\partial t}\cdot\mathbf{v}_h\,\mathrm{d}\mathbf{x}. \tag{45}$$

The nodal states $\mathbf{u}_i(t) = \mathbf{u}_h(\mathbf{x}_i,t)$ are uniformly bounded by assumption and satisfy the semi-discrete energy inequality (19). The Lipschitz continuity of the numerical flux function $\mathcal{Q}$ implies that the time derivative of $\mathbf{u}_h$ is uniformly bounded as well. Therefore, the first term on the right-hand side of (45) vanishes as $h \to 0$. To estimate the second term, we follow the proof of Lax–Wendroff consistency in Theorem 2. Invoking (32a) and using the assumption that $\nabla\cdot\mathbf{v} = 0$, we arrive at

$$\int_\Omega \frac{\partial\mathbf{u}_h}{\partial t}\cdot\mathbf{v}\,\mathrm{d}\mathbf{x} = \int_\Omega (\mathbf{u}_h\otimes\mathbf{u}_h) : \nabla\mathbf{v}\,\mathrm{d}\mathbf{x} + e_{\mathbf{u}_h}(\mathbf{v},t),$$

where

$$\begin{aligned} e_{\mathbf{u}_h}(\mathbf{v},t) = {} & \int_\Omega \frac{\partial\mathbf{u}_h}{\partial t}\cdot(\mathbf{v}-\mathbf{v}_h)\,\mathrm{d}\mathbf{x} + \left(\frac{\partial\mathbf{u}_h}{\partial t},\mathbf{v}_h\right)_{L^2(\Omega)} - \left(\frac{\partial\mathbf{u}_h}{\partial t},\mathbf{v}_h\right)_{L_h^2(\Omega)} \\ & - \int_\Omega (\mathbf{u}_h\otimes\mathbf{u}_h) : \nabla\mathbf{v}_h\,\mathrm{d}\mathbf{x} - a(\mathbf{u}_h,\mathbf{v}_h) + s_h^u(\mathbf{u}_h,\mathbf{v}_h) \\ & + b(\mathbf{v}-\mathbf{v}_h,p_h) - \int_\Omega (\mathbf{u}_h\otimes\mathbf{u}_h) : \nabla(\mathbf{v}-\mathbf{v}_h)\,\mathrm{d}\mathbf{x}. \end{aligned}$$

The first term on the right-hand side of the formula for $e_{\mathbf{u}_h}(\mathbf{v},t)$ has already been estimated in (45). The remainder of the first line represents the consistency error due to mass lumping. It can again be estimated as in [35, Thm. 3]. The second line is the consistency error associated with the discretization of the nonlinear convective term. By Lemmas 4 and 5, this error tends to zero as $h \to 0$. The term $b(\mathbf{v}-\mathbf{v}_h,p_h)$ measures the divergence error in the interpolant $\mathbf{v}_h = I_h\mathbf{v}$. It can be estimated using the Cauchy–Schwarz inequality and the interpolation error estimate $\|\nabla\cdot(\mathbf{v}-\mathbf{v}_h)\|_{L^2(\Omega)} \le Ch|\mathbf{v}|_{H^2(\Omega)}$. The second term in the third line can be estimated similarly. Combining the above estimates for the individual components of $e_{\mathbf{u}_h}(\mathbf{v},t)$, we complete the proof of the theorem. □

Finally, the assumptions of the following theorem guarantee weak convergence to a DMV solution.

Theorem 4 (*Weak Convergence*)**.** *Assume that Lemmas 1–5 are applicable on a time interval $[0,T]$ and let the initial data $\mathbf{u}_{h,0}$ be admissible. Consider a family $\{\mathbf{U}_h\}_{h\searrow 0} \equiv \{\mathbf{u}_h,p_h\}_{h\searrow 0}$ of uniformly bounded numerical solutions obtained with the scheme (32). Then there exists a subsequence of $\mathbf{U}_h$ (denoted again by $\mathbf{U}_h$) such that*

$$\mathbf{u}_h \to \langle \mathcal{U}_{(\mathbf{x},t)}; \tilde{\mathbf{u}}\rangle \text{ weakly}-* \text{ in } L^\infty((0,T);L^2(\Omega;\mathbb{R}^d))$$

as $h \to 0$. The limit $\mathcal{U}_{(\mathbf{x},t)}$ is a DMV solution of the incompressible Euler equations corresponding to the initial data $\mathbf{u}_0$ and concentration defects

$$D_{cd}(t) = \overline{\eta(\mathbf{u})}(t) - \frac{1}{2}\langle \mathcal{U}_{(\mathbf{x},t)}; |\tilde{\mathbf{u}}|^2\rangle, \qquad \mathfrak{M}_{cd}(t) = \overline{\mathbf{u}\otimes\mathbf{u}} - \langle \mathcal{U}_{(\mathbf{x},t)}; \tilde{\mathbf{u}}\otimes\tilde{\mathbf{u}}\rangle,$$

where $\overline{\eta(\mathbf{u})}$ is the weak-$*$ limit of $\eta(\mathbf{u}_h) = \frac{1}{2}|\mathbf{u}_h|^2$ as $h \to 0$ in $L^\infty(0,T;\mathcal{M}^+(\Omega))$ and $\mathbf{u}\otimes\mathbf{u}$ is the weak-$*$ limit of $\{\mathbf{u}_h\otimes\mathbf{u}_h\}_h$ in $L^\infty(0,T;\mathcal{M}(\Omega;\mathbb{R}^{d\times d}))$.

Proof. The result of Theorem 4 does not rely on any details of the discretization procedure. Instead, the proof technique that we use in this work exploits the inherent properties of our structure-preserving numerical scheme. In view of the consistency result that they imply, we can closely follow the convergence proof outlined in [55]. Its central idea involves leveraging the uniform boundedness of various quantities, applying the Fundamental Theorem of Young measures, and using the consistency estimates provided by Theorem 3. □

Remark 8 (*Discussion on Convergence and Physical Interpretation of DMV Solutions*)**.** Weak Weak convergence of approximate solutions is difficult

to verify and visualize in numerical studies. Therefore, the concept of *$\mathscr{K}$-convergence* for Young measures has been adapted to this purpose by Feireisl et al. [74] who showed, among other things, pointwise convergence of arithmetic averages (Cesaro means) of numerical solutions to a generalized dissipative weak solution of the limit system.

In addition, if we have more information on the regularity of the underlying solutions, strong convergence, i.e., classical grid convergence, of a sequence of approximate solutions can also be investigated. Both strong convergence and $\mathscr{K}$ convergence can then be shown similarly to the compressible/hyperbolic case. For technical details, we refer the interested reader to [33,35,55].

A heuristic interpretation of DMV solutions in the context of fluid flows is as follows: The DMV framework makes it possible to describe fluid motion when more traditional solution concepts, e.g., that of classical solutions, fail, especially in the presence of turbulence or other fine-scale phenomena. The deterministic notion of classical/weak solutions is extended by allowing the velocity field and related quantities to be described as probability distributions at each point in space and time, capturing oscillations and fluctuations that are characteristic, for example, of turbulent flows. By incorporating oscillation and concentration defects, DMV solutions bridge the gap between the macroscopic fluid behavior and unresolved microscopic phenomena, trying to provide a consistent description across scales. For more information, we refer to [75] and the references therein.

5. Numerical results

We apply our locally energy-stable finite element method (15) with $d_{ij}^u = 0$ to standard 2D test problems in this section. Following Becker and Hansbo [51], the pressure stabilization parameter ω is set to 0.5 in all experiments. Our implementation invokes mesh generation techniques from the open-source packages FESTUNG [76,77] and MFEM [78,79]. In a postprocessing step, periodicity is enforced by manipulating the grid data as required. This task is accomplished by identifying nodes (and also edges, depending on the implementation/discretization) that represent the same entity on periodic domains. The numerical approximations are visualized with the open-source software GLVis [80]. Initial conditions for the velocity vector are generated via consistent $L^2(\Omega)$ projections (by default) or lumped $L^2(\Omega)$ projections if the initial conditions are nonsmooth (Gresho vortex, Section 5.2).

5.1. Taylor–Green vortex

First, we assess the accuracy of the method under investigation by running the Taylor–Green vortex test in $\Omega = (0,1)^2$. The smooth exact solution to this incompressible flow problem reads [81]

$$\mathbf{u}(x,y,t) = \begin{bmatrix} \sin(2\pi x)\sin(2\pi y) \\ \cos(2\pi x)\cos(2\pi y) \end{bmatrix} \exp(-8\pi^2 \nu t), \tag{46}$$

$$p(x,y,t) = \frac{1}{2}[1 - \sin^2(2\pi x) - \cos^2(2\pi y)]\exp(-16\pi^2\nu t).$$

Note that $\int_\Omega p(x,y,t)\mathrm{d}x\mathrm{d}y = 0$ for all $t \geq 0$. Following [81, Sec. 4.3], we set $\nu = 10^{-5}$ and run simulations up to the end time $t = 1$, at which we compute the $L^2(\Omega)$ errors $e_{\mathbf{u}}^M$, e_p^M in the velocity $\mathbf{u}$ and pressure p. The superscript $M \in \{C, L\}$ indicates whether calculations are performed with the consistent or lumped mass matrix. Using a hierarchy of uniform Friedrichs–Keller triangulations, unstructured Delaunay meshes and uniform quadrilateral grids, we calculate the experimental orders of convergence (EOC). The ratio $\Delta t/h$, where $h = \max_e \mathrm{diam}(K^e)$, is kept fixed in each case with values of $\Delta t/h = \sqrt{2}/4 \approx 0.3536$ for both types of structured grids and $\Delta t/h = 5/16 = 0.3125$ for computations on unstructured meshes. These choices amount to a total of 512 time steps on the finest mesh of each type. The results of our grid convergence study are presented in Tables 1–3.

We observe that both the lumped and the consistent mass matrix versions of our scheme converge with optimal orders of accuracy in every variable. To further quantify the dissipative properties of the new discretizations, we track the temporal evolutions of kinetic energies and compare them with the exact energy. According to (46), the latter decays exponentially in time at the rate of $-16\pi^2\nu$. Since the kinetic energies of discrete initial data are generally mesh dependent, we normalize the data sets by their respective initial values. The results are presented in Fig. 1. Note that the kinetic energies of lumped and consistent mass matrix approximations are computed differently, namely as follows:

$$\eta_L(\mathbf{u}_h) = \frac{1}{2}(\mathbf{u}_h, \mathbf{u}_h)_{L^2(\Omega)}, \qquad \eta_C(\mathbf{u}_h) = \frac{1}{2}(\mathbf{u}_h, \mathbf{u}_h)_{L_h^2(\Omega)}.$$

Generally, the lumped-mass solutions seem to be less diffusive than their consistent-mass counterparts. This observation is illustrated by the error behavior in Tables 1–3. Upon spatial and temporal refinement, each profile converges to that for the exact energy evolution. While the analysis presented in Section 3 guarantees that the total energy is nonincreasing for the semi-discrete scheme and exact time integration, our numerical results indicate that the global energy stability property carries over to the fully discrete setting. Indeed, all profiles obtained in this study are monotonically decreasing.

Next, we study the long-time solution behavior by running the simulations up to an end time that is 50 times larger than before. Again, we use lumped and consistent mass matrices, as well as the three types of meshes. In Figs. 2–3, we present snapshots of the velocity magnitude and pressure obtained with the lumped-mass version of our scheme on the finest level of a structured quadrilateral grid. The numerical solutions obtained with any of the other five computational setups are qualitatively similar to the displayed approximations. Kinetic energy profiles for all runs are shown in Fig. 4.

In Figs. 2–3, we observe the so-called inverse cascade. The originally coherent vortical structures of the Taylor cells, as seen in Figs. (a) and (b), undergo a self-organization after a startup phase (here after $t = 35$). The resulting flow patterns are depicted in Figs. (c)–(h); see also [82]. A mathematical discussion of such self-organization in 2D turbulent incompressible flows can be found in [83].

5.2. Gresho vortex

Next, we solve a test problem with a nonsmooth solution, known as the Gresho vortex [84,85]. The physical viscosity ν is zero in this experiment. That is, we are now considering the incompressible Euler limit (38) of (1). The exact solution coincides with the initial data, which is defined as follows:

$$r(x,y) = \sqrt{x^2+y^2}, \qquad \mathbf{u}(x,y) = (-y,x)\begin{cases} 5 & \text{if } r(x,y) \leq \frac{1}{5}, \\ \frac{2}{r(x,y)} - 5 & \text{if } \frac{1}{5} \leq r(x,y) \leq \frac{2}{5}, \\ 0 & \text{otherwise,} \end{cases}$$

$$p(x,y) = \begin{cases} 5 + \frac{25}{2}r(x,y)^2 & \text{if } r(x,y) \leq \frac{1}{5}, \\ 9 - 4\log\left(\frac{1}{5}\right) + \frac{25}{2}r(x,y)^2 - 20r(x,y) + 4\log(r(x,y)) & \text{if } \frac{1}{5} \leq r(x,y) \leq \frac{2}{5}, \\ 3 + 4\log(2) & \text{otherwise.} \end{cases}$$

The purpose of this popular 2D test is to check how well the method under investigation can preserve the exact steady state. Note that the velocity is of class C^0, while the pressure is of class C^1. Therefore, second-order convergence for the pressure is possible, while, according to [84], the empirical convergence rate for the velocity is around 1.4. We also remark that we need to normalize p in the above definition to satisfy the zero mean condition. To this end, we subtract $p_0 = \int_\Omega p(x,y)\mathrm{d}x\mathrm{d}y$ from p. The value of p_0 can be accurately evaluated by subdividing Ω and changing to polar coordinates.

We run the same experiments as for the Taylor–Green vortex at the beginning of Section 5.1. The computational domain is chosen to be

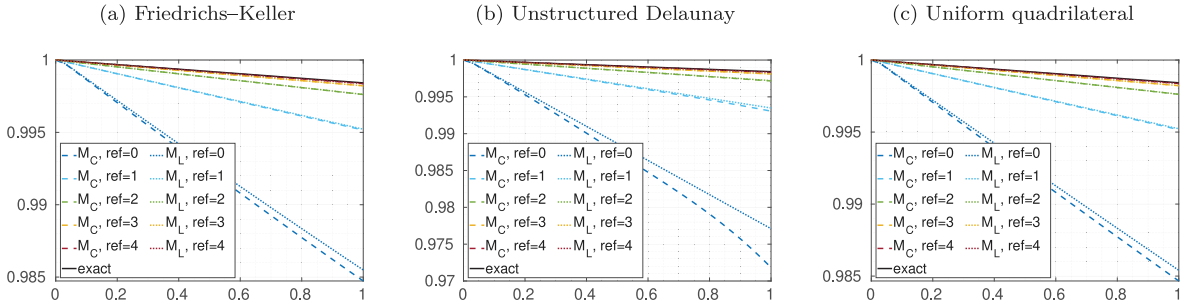

Fig. 1. Energy evolutions for the Taylor–Green vortex, exact profile and numerical results obtained on refinement levels `ref` for three types of meshes.

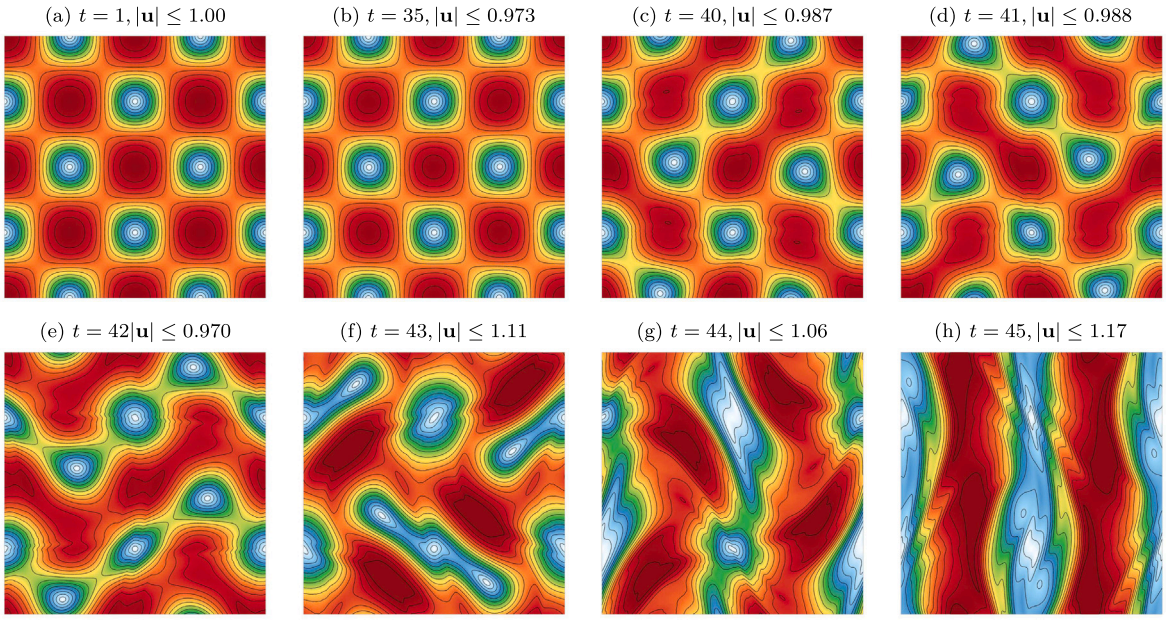

Fig. 2. Snapshots of finite element approximations to $|\mathbf{u}|$ for the Taylor–Green vortex obtained on a uniform quadrilateral mesh with 256 × 256 elements using the lumped mass matrix and the time step $\Delta t = 1/512$.

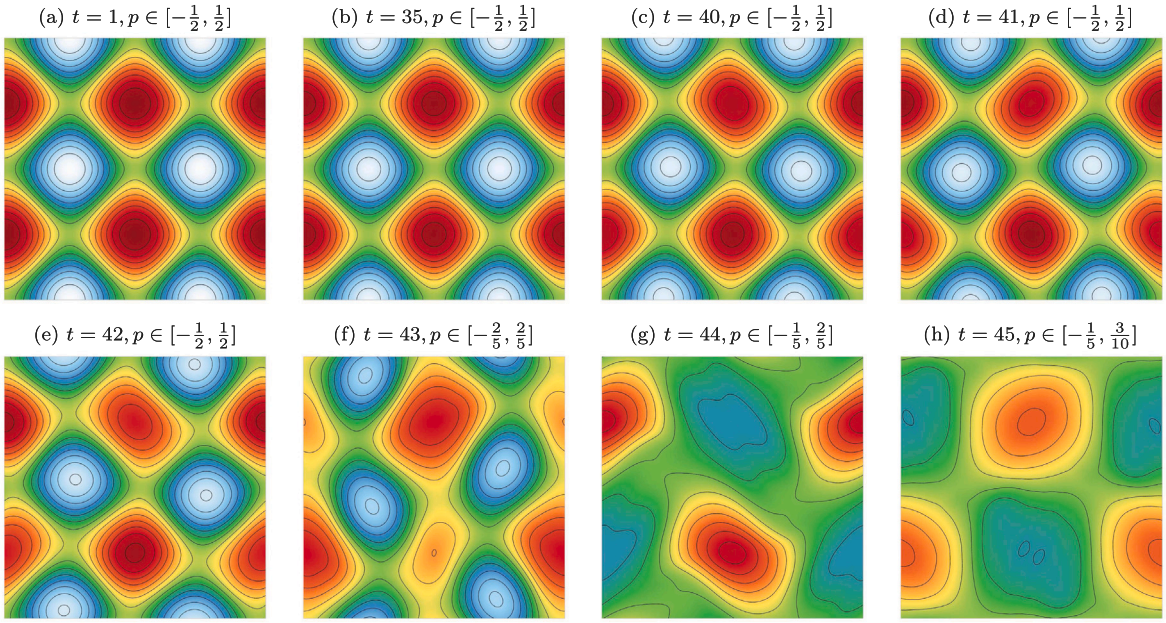

Fig. 3. Snapshots of finite element approximations to p for the Taylor–Green vortex obtained on a uniform quadrilateral mesh with 256 × 256 elements using the lumped mass matrix and $\Delta t = 1/512$.

Table 1
$L^2(\Omega)$ convergence for the Taylor–Green vortex on Friedrichs–Keller triangulations.

$\sqrt{2}/h$	$e^C_{\mathbf{u}}$	EOC	e^C_p	EOC	$e^L_{\mathbf{u}}$	EOC	e^L_p	EOC
16	8.01E−02		6.59E−03		6.75E−02		5.74E−03	
32	1.90E−02	2.08	1.37E−03	2.26	1.82E−02	1.89	1.35E−03	2.09
64	4.77E−03	2.00	3.55E−04	1.95	4.71E−03	1.95	3.53E−04	1.93
128	1.20E−03	1.99	9.03E−05	1.98	1.20E−03	1.98	9.03E−05	1.97
256	3.02E−04	1.99	2.28E−05	1.99	3.02E−04	1.99	2.28E−05	1.98
average		2.02		2.05		1.95		1.99

Table 2
$L^2(\Omega)$ convergence for the Taylor–Green vortex on unstructured Delaunay meshes.

$1/h$	$e^C_{\mathbf{u}}$	EOC	e^C_p	EOC	$e^L_{\mathbf{u}}$	EOC	e^L_p	EOC
10	2.50E−01		1.20E−01		6.24E−02		2.98E−02	
20	7.58E−02	1.72	2.93E−02	2.03	2.16E−02	1.53	9.07E−03	1.71
40	2.32E−02	1.71	8.82E−03	1.73	7.40E−03	1.55	3.15E−03	1.53
80	6.92E−03	1.75	2.09E−03	2.07	2.50E−03	1.56	9.93E−04	1.66
160	1.18E−03	2.55	4.68E−04	2.16	8.13E−04	1.62	3.06E−04	1.70
average		1.93		2.00		1.57		1.65

Table 3
$L^2(\Omega)$ convergence for the Taylor–Green vortex on uniform quadrilateral grids.

$\sqrt{2}/h$	$e^C_{\mathbf{u}}$	EOC	e^C_p	EOC	$e^L_{\mathbf{u}}$	EOC	e^L_p	EOC
16	8.83E−03		4.59E−03		7.38E−03		4.22E−03	
32	2.11E−03	2.07	1.01E−03	2.19	2.00E−03	1.88	9.77E−04	2.11
64	5.23E−04	2.01	2.44E−04	2.05	5.16E−04	1.96	2.42E−04	2.01
128	1.31E−04	2.00	6.07E−05	2.00	1.30E−04	1.99	6.07E−05	2.00
256	3.27E−05	2.00	1.53E−05	1.99	3.26E−05	2.00	1.53E−05	1.99
average		2.02		2.08		1.96		2.03

Table 4
$L^2(\Omega)$ convergence for the Gresho vortex on Friedrichs–Keller triangulations.

$\sqrt{2}/h$	$e^C_{\mathbf{u}}$	EOC	e^C_p	EOC	$e^L_{\mathbf{u}}$	EOC	e^L_p	EOC
16	5.92E−02		2.23E−02		5.01E−02		2.15E−02	
32	1.95E−02	1.60	6.40E−03	1.80	1.72E−02	1.54	6.09E−03	1.82
64	7.02E−03	1.48	1.58E−03	2.02	5.55E−03	1.63	1.52E−03	2.00
128	2.54E−03	1.47	3.82E−04	2.05	1.84E−03	1.59	3.74E−04	2.02
256	9.67E−04	1.39	9.37E−05	2.03	6.56E−04	1.48	9.21E−05	2.02
average		1.49		1.98		1.56		1.97

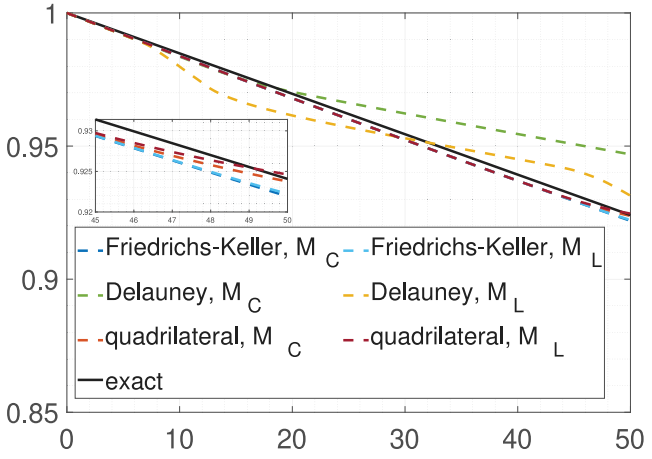

Fig. 4. Long-term energy evolutions for the Taylor–Green vortex on finest meshes.

$\Omega = (-0.5, 0.5)^2$, which yields $p_0 \approx 5.688812918144054$. Simulations are terminated at the pseudo-time $t = 1$. We use the same combinations of meshes and time steps as in Section 5.1. The results of this grid convergence study are presented in Tables 4–6.

Additionally, we track the kinetic energy evolution in pseudo-time for all runs. The results shown in Fig. 5 are consistent with the findings from Section 5.1. While the exact energy is constant at steady state, all numerical approximations are dissipating energy. This issue cannot be avoided because for nonconstant velocities (as in this test), some of the symmetric terms G_{ij} that appear in (23) are nonzero, and energy is therefore lost over time. Increased resolution reduces these errors, and optimal convergence rates are attained for the velocity and pressure approximations. Snapshots of the velocity magnitude and pressure at $t = 1$ obtained on the finest Delaunay mesh are displayed in Fig. 6.

The Gresho vortex is also a perfect example for illustrating the necessity of using stabilization techniques. To show the superiority of (15) over (7), we ran additional tests for a combination of the Galerkin space discretization with implicit-explicit (IMEX) time stepping of Euler type. In the so-defined fully discrete scheme, the nonlinear convective term $(\varphi_i, \mathbf{u}_h \cdot \nabla \mathbf{u}_h)_{L^2(\Omega)}$ is treated explicitly, as in the forward Euler version, while all other terms are treated implicitly, as in the backward Euler version. In our numerical studies for the Galerkin IMEX-Euler method with consistent and lumped mass matrices, we use a coarse Friedrichs–Keller triangulation with $h = \sqrt{2}/32$ in combination with time steps $\Delta t = 0.5^k$, where $k \in \{6, 8, 10, 12\}$. Note that for the finest time step, the ratio $\Delta t/h \approx 0.0055$ is already extremely small. The energy curves for this experiment are displayed in Fig. 7 along with the discrete initial distribution of the velocity magnitude. For each of the eight runs, there exists a time at which kinetic energy starts growing and, as a consequence, numerical instabilities arise. We

Table 5
$L^2(\Omega)$ convergence for the Gresho vortex on unstructured Delaunay meshes.

$1/h$	$e^C_{\mathbf{u}}$	EOC	e^C_p	EOC	$e^L_{\mathbf{u}}$	EOC	e^L_p	EOC
10	1.13E−01		4.23E−02		5.67E−02		2.83E−02	
20	3.72E−02	1.60	1.02E−02	2.05	2.35E−02	1.27	8.77E−03	1.69
40	1.37E−02	1.44	2.51E−03	2.02	8.57E−03	1.45	2.30E−03	1.93
80	5.18E−03	1.40	7.18E−04	1.81	3.02E−03	1.51	5.97E−04	1.95
160	1.78E−03	1.54	1.71E−04	2.07	1.13E−03	1.42	1.59E−04	1.91
average		1.50		1.99		1.41		1.87

Table 6
$L^2(\Omega)$ convergence for the Gresho vortex on uniform quadrilateral grids.

$\sqrt{2}/h$	$e^C_{\mathbf{u}}$	EOC	e^C_p	EOC	$e^L_{\mathbf{u}}$	EOC	e^L_p	EOC
16	4.34E−02		2.02E−02		3.99E−02		1.95E−02	
32	1.44E−02	1.59	5.55E−03	1.86	1.31E−02	1.61	5.41E−03	1.85
64	5.32E−03	1.44	1.46E−03	1.93	4.76E−03	1.46	1.40E−03	1.94
128	1.78E−03	1.58	3.69E−04	1.98	1.60E−03	1.58	3.61E−04	1.96
256	6.81E−04	1.39	9.00E−05	2.03	5.91E−04	1.43	8.89E−05	2.02
average		1.50		1.95		1.52		1.94

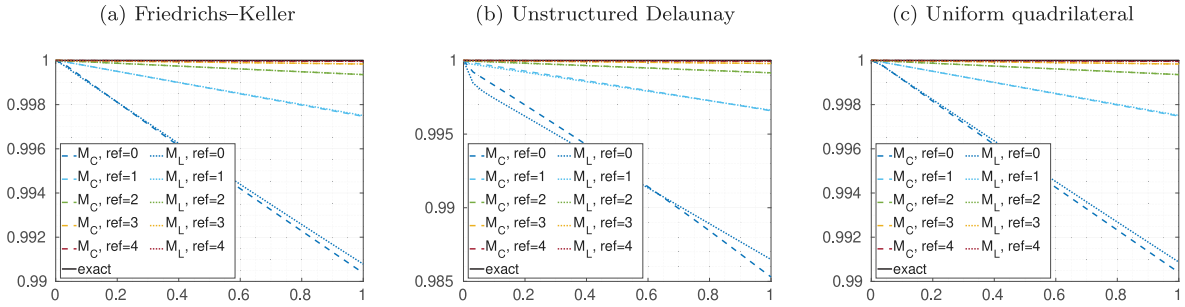

Fig. 5. Energy evolutions for the Gresho vortex, exact profile and numerical results obtained on refinement levels `ref` for three types of meshes.

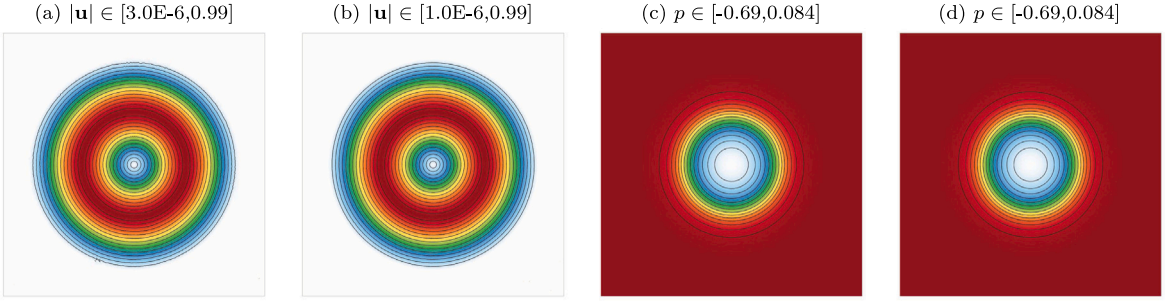

Fig. 6. Finite element approximations to $|\mathbf{u}|$ and p for the Gresho vortex at $t = 1$ obtained on the finest level of the unstructured Delaunay mesh using the consistent (panels a,c) and lumped (panels b,d) mass matrices.

observe severe blowups, as the energy quickly tends to infinity, thus rendering the corresponding approximations useless. As before, lumping of mass matrices is beneficial for the unstable $\mathbb{P}_1\mathbb{P}_1$ discretization, which manifests itself in the fact that the instabilities occur later than in the corresponding consistent mass matrix runs. In our experience, breakdowns and blowups due to spurious energy production can only be delayed to some extent but not avoided altogether without energy stabilization.

In contrast, our new energy-stable schemes can be run with arbitrarily large time steps and still produce stable results. The use of large pseudo-time steps Δt yields harder-to-solve linear systems because small time steps lead to dominant mass matrix contributions. However, fewer updates produce less diffusive approximations to steady-state solutions. To quantify these effects, we ran the Gresho test again up to end time $t = 1000$ with all three types of meshes using $h = 1/128$ for the structured grids and $h = 1/80$ in the case of the unstructured Delaunay triangulation. In Tables 7–8, we display the total time required for computations using $\Delta t \in \{1, 1000\}$ and both kinds of mass matrices. To give an indication of how diffusive each approach is, we also report the maximum velocity magnitude and relative energy loss. Note that $\Delta t = 1$ is already larger by a factor of 256 than the corresponding time step employed in the earlier convergence studies for the same grids. For accuracy reasons, the use of time steps as large (compared to the mesh size) as in the present experiments is naturally discouraged for transient problems. Our only reason for including the elapsed times here is to facilitate a comparison of the linear solver's performance for $\Delta t = 1$ vs. $\Delta t = 1000$. Thus, we refrain from repeating various runs with the same numerical parameters or testing different hardware.

Despite the fact that the time step $\Delta t = 1000$ is extremely large, the corresponding approximations on structured grids agree qualitatively well with the ones shown in Fig. 6. On the unstructured mesh, the pressure solution is in reasonable agreement with the exact solution, while the velocity field contains nonphysical artifacts. All results obtained with $\Delta t = 1$ are useless because temporal discretization errors

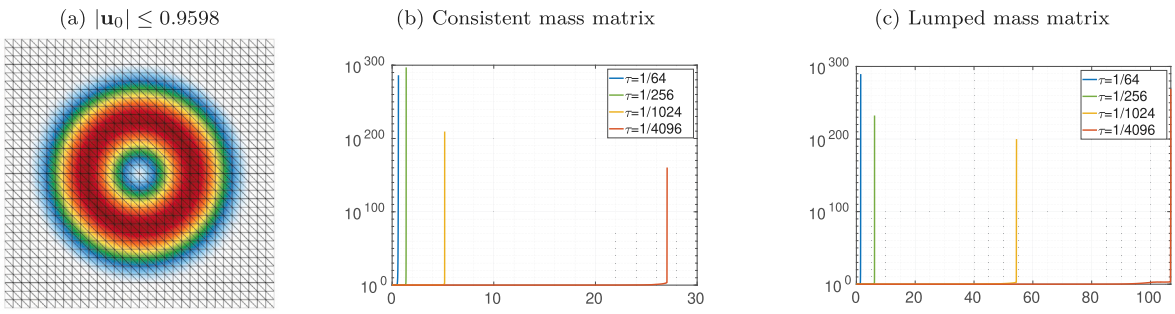

Fig. 7. Gresho vortex results for the non-stabilized Galerkin IMEX-Euler discretization on a Friedrichs–Keller triangulation with $h = \sqrt{2}/32$. The diagrams show a mesh plot of the discrete initial data (panel a) and semi-logarithmic plots of energy evolutions for simulations using the consistent (panel b) and lumped (panel c) mass matrices.

Table 7
Gresho vortex problem solved up to $t = 1000$ using $\Delta t = 1$.

Discretization	Time [s]	$\max_{\mathbf{x}\in\Omega} \lvert\mathbf{u}_h(\mathbf{x}, t = 1000)\rvert$	Energy loss %
Friedrichs–Keller, consistent	655	0.947	80.9
Friedrichs–Keller, lumped	655	0.690	72.7
unstructured Delaunay, consistent	576	1.22	77.2
unstructured Delaunay, lumped	577	0.864	70.5
uniform quadrilateral, consistent	710	1.48	72.6
uniform quadrilateral, lumped	722	0.794	64.0

Table 8
Gresho vortex problem solved up to $t = 1000$ using $\Delta t = 1000$.

Discretization	Time [s]	$\max_{\mathbf{x}\in\Omega} \lvert\mathbf{u}_h(\mathbf{x}, t = 1000)\rvert$	Energy loss %
Friedrichs–Keller, consistent	41.1	0.930	7.66
Friedrichs–Keller, lumped	21.3	0.929	7.65
unstructured Delaunay, consistent	21.0	3.82	9.28
unstructured Delaunay, lumped	8.72	2.92	9.06
uniform quadrilateral, consistent	62.9	0.925	7.66
uniform quadrilateral, lumped	64.0	0.926	7.65

of order $\mathcal{O}(\Delta t^3) = \mathcal{O}(1)$ arise in each time step and accumulate over time. The resulting velocity and pressure fields are oscillatory and bear no resemblance to the exact solution. However, the proposed scheme remains stable with large percentages of energy being dissipated.

The large time step experiments for the Gresho vortex are meant to demonstrate the stability of our new scheme and the performance of the linear solvers in the context of steady-state computations. The occurrence of bounded spurious oscillations does not contradict the theory developed in Sections 3 and 4 for the energy-stable space discretization (20). The use of very large time steps in fully discrete schemes may result in numerical artifacts due to unacceptable rates of local energy production. However, no increase in the total energy was observed in any of our numerical experiments.

Slight differences in the computational time and diffusivity for discretizations listed in Tables 7 and 8 are due to varying spatial resolution. It is interesting to note that in the experiment using $\Delta t = 1000$, the lumped-mass version is more efficient for triangular grids than for quadrilaterals. Moreover, Friedrichs–Keller triangulations seem to outperform quadrilateral grids despite employing the same number of unknowns and yielding results of comparable accuracy. These cost factors can be attributed to the linear solver (MATLAB's backslash operator), which we found to be the bottleneck that dominates the computational cost of our current implementation. The computational time for a simulation run using 1000 time steps by far exceeds the cost of a computation using a single time step. Clearly, this is due to the need for solving many linear systems instead of just one. Normalized by the factor 1000, however, the computational cost per time step is clearly much less for $\Delta t = 1$. This confirms that the use of inordinately large time steps may significantly degrade the conditioning of system matrices and increase the overall computational effort for solving linear systems. Moreover, we ran into memory issues not encountered for $\Delta t = 1$ when we tried to use $\Delta t = 1000$ on even finer grids.

6. Conclusions

The main focus of this work was on the theoretical and practical implications of local energy inequalities in the context of (continuous $\mathbb{P}_1\mathbb{P}_1$) finite element methods for incompressible flow problems. The proposed methodology has a lot in common with algebraic flux correction schemes for nonlinear hyperbolic systems, which enables us to exploit the existing similarities. The results of our theoretical studies and numerical experiments illustrate the importance of local energy stability, which we use as a tool for proving consistency and convergence towards dissipative weak solutions. It is hoped that our findings provide strong motivation for further research efforts in the field of structure-preserving finite element schemes for the incompressible Navier–Stokes equations. We finally remark that the design of locally energy stable high-order extensions is likely to require subcell flux correction (as in [27,28]) and more sophisticated analysis or the use of alternative energy stabilization procedures.

CRediT authorship contribution statement

Hennes Hajduk: Writing – original draft, Visualization, Software, Investigation, Formal analysis. **Dmitri Kuzmin:** Writing – original draft, Methodology, Formal analysis, Conceptualization. **Gert Lube:** Writing – review & editing. **Philipp Öffner:** Writing – original draft, Formal analysis.

Declaration of competing interest

The authors declare that they have no known competing financial interests or personal relationships that could have appeared to influence the work reported in this paper.

Acknowledgments

The work of D.K. and P.Ö. was supported by the German Research Foundation (DFG), Germany within the framework of the priority research program SPP 2410 under grants KU 1530/30-1 and OE 661/5-1, respectively. P.Ö. was also supported by the DFG, Germany under the personal grant 520756621 (OE 661/4-1).

H.H. acknowledges support from The Rough Ocean Project, funded by the Research Council of Norway under the Klimaforsk-programme, Project 302743. H.H. also thanks Dr. Christoph Lohmann (TU Dortmund University) for a helpful suggestion on how to efficiently assemble certain operators.

Data availability

Data will be made available on request.

References

[1] Kuzmin D, Hajduk H. Property-preserving numerical schemes for conservation laws. World Scientific; 2023.
[2] Kuzmin D, Möller M, Gurris M. Algebraic flux correction II. Compressible flow problems. In: Kuzmin D, Löhner R, Turek S, editors. Flux-corrected transport: principles, algorithms, and applications. second ed.. Springer; 2012, p. 193–238.
[3] Kuzmin D, Möller M, Shadid JN, Shashkov M. Failsafe flux limiting and constrained data projections for equations of gas dynamics. J Comput Phys 2010;229(23):8766–79.
[4] Löhner R, Morgan K, Peraire J, Vahdati M. Finite element flux-corrected transport (FEM-FCT) for the Euler and Navier–Stokes equations. Internat J Numer Methods Fluids 1987;7(10):1093–109.
[5] Jameson A. Computational algorithms for aerodynamic analysis and design. Appl Numer Math 1993;13(5):383–422.
[6] Jameson A. Positive schemes and shock modelling for compressible flows. Internat J Numer Methods Fluids 1995;20(8–9):743–76.
[7] Lyra PRM, Morgan K. A review and comparative study of upwind biased schemes for compressible flow computation. III: Multidimensional extension on unstructured grids. Arch Comput Methods Eng 2002;9:207–56.
[8] Bouchut F. Nonlinear stability of finite volume methods for hyperbolic conservation laws and well-balanced schemes for sources. Birkhäuser; 2004.
[9] Chandrashekar P. Kinetic energy preserving and entropy stable finite volume schemes for compressible Euler and Navier–Stokes equations. Commun Comput Phys 2013;14(5):1252–86.
[10] Coppola G, Veldman AEP. Global and local conservation of mass, momentum and kinetic energy in the simulation of compressible flow. J Comput Phys 2023;475:111879.
[11] Hillebrand D, Klein S-C, Öffner P. Applications of limiters, neural networks and polynomial annihilation in higher-order FD/FV schemes. J Sci Comput 2023;97(1):13.
[12] Jameson A. Formulation of kinetic energy preserving conservative schemes for gas dynamics and direct numerical simulation of one-dimensional viscous compressible flow in a shock tube using entropy and kinetic energy preserving schemes. J Sci Comput 2008;34(2):188–208.
[13] Ortleb S. A kinetic energy preserving DG scheme based on Gauss–Legendre points. J Sci Comput 2017;71(3):1135–68.
[14] Ray D, Chandrashekar P, Fjordholm US, Mishra S. Entropy stable scheme on two-dimensional unstructured grids for Euler equations. Commun Comput Phys 2016;19(5):1111–40.
[15] Subbareddy PK, Candler GV. A fully discrete, kinetic energy consistent finite-volume scheme for compressible flows. J Comput Phys 2009;228(5):1347–64.
[16] Tadmor E. Entropy stability theory for difference approximations of nonlinear conservation laws and related time-dependent problems. Acta Numer 2003;12:451–512.
[17] Kuzmin D. Algebraic flux correction I. Scalar conservation laws. In: Kuzmin D, Löhner R, Turek S, editors. Flux-corrected transport: principles, algorithms, and applications. second ed.. Springer; 2012, p. 145–92.
[18] Carlier V, Renac F. Invariant domain preserving high-order spectral discontinuous approximations of hyperbolic systems. SIAM J Sci Comput 2023;45(3):A1385–412.
[19] Guermond J-L, Nazarov M, Popov B, Tomas I. Second-order invariant domain preserving approximation of the Euler equations using convex limiting. SIAM J Sci Comput 2018;40(5):A3211–39.
[20] Kuzmin D. Monolithic convex limiting for continuous finite element discretizations of hyperbolic conservation laws. Comput Methods Appl Mech Engrg 2020;361:112804.
[21] Zhang X, Shu C-W. Maximum-principle-satisfying and positivity-preserving high-order schemes for conservation laws: Survey and new developments. Proc R Soc A: Math Phys Eng Sci 2011;467(2134):2752–76.
[22] Dobrev V, Kolev T, Kuzmin D, Rieben R, Tomov V. Sequential limiting in continuous and discontinuous Galerkin methods for the Euler equations. J Comput Phys 2018;356:372–90.
[23] Lohmann C, Kuzmin D. Synchronized flux limiting for gas dynamics variables. J Comput Phys 2016;326:973–90.
[24] Gassner GJ. A skew-symmetric discontinuous Galerkin spectral element discretization and its relation to SBP-SAT finite difference methods. SIAM J Sci Comput 2013;35(3):A1233–53.
[25] Kuzmin D, Hajduk H, Rupp A. Limiter-based entropy stabilization of semi-discrete and fully discrete schemes for nonlinear hyperbolic problems. Comput Methods Appl Mech Engrg 2022;389:114428.
[26] Pazner W, Persson P-O. Analysis and entropy stability of the line-based discontinuous Galerkin method. J Sci Comput 2019;80(1):376–402.
[27] Hajduk H. Monolithic convex limiting in discontinuous Galerkin discretizations of hyperbolic conservation laws. Comput Math Appl 2021;87:120–38.
[28] Kuzmin D, Quezada de Luna M. Subcell flux limiting for high-order Bernstein finite element discretizations of scalar hyperbolic conservation laws. J Comput Phys 2020;411:109411.
[29] Lin Y, Chan J. High order entropy stable discontinuous Galerkin spectral element methods through subcell limiting. J Comput Phys 2024;498:112677.
[30] Pazner W. Sparse invariant domain preserving discontinuous Galerkin methods with subcell convex limiting. Comput Methods Appl Mech Engrg 2021;382:113876.
[31] Rueda-Ramírez AM, Bolm B, Kuzmin D, Gassner GJ. Monolithic convex limiting for Legendre–Gauss–Lobatto discontinuous Galerkin spectral-element methods. Commun Appl Math Comput 2024;6:1860–98.
[32] Feireisl E, Lukáčová-Medvid'ová M, Mizerová H. Convergence of finite volume schemes for the Euler equations via dissipative measure-valued solutions. Found Comput Math 2020;20(4):923–66.
[33] Feireisl E, Lukáčová-Medvid'ová M, Mizerová H, She B. Numerical analysis of compressible fluid flows. Springer; 2021.
[34] Abgrall R, Lukáčová-Medvid'ová M, Öffner P. On the convergence of residual distribution schemes for the compressible Euler equations via dissipative weak solutions. Math Models Methods Appl Sci 2023;33(1):139–73.
[35] Kuzmin D, Lukáčová-Medvid'ová M, Öffner P. Consistency and convergence of flux-corrected finite element methods for nonlinear hyperbolic problems. 2023, Preprint: https://arxiv.org/abs/2308.14872 [math.NA].
[36] Lukáčová-Medvid'ová M, Öffner P. Convergence of discontinuous Galerkin schemes for the Euler equations via dissipative weak solutions. Appl Math Comput 2023;436:127508.
[37] Boris JP, Grinstein FF, Oran ES, Kolbe RL. New insights into large eddy simulation. Fluid Dyn Res 1992;10(4–6):199.
[38] Drikakis D, Rider W. High-resolution methods for incompressible and low-speed flows. Springer; 2005.
[39] Grinstein FF, Fureby C. From canonical to complex flows: Recent progress on monotonically integrated LES. Comput Sci Engrg 2004;6(2):36–49.
[40] Grinstein FF, Fureby C. On monotonically integrated large eddy simulation of turbulent flows based on FCT algorithms. In: Kuzmin D, Löhner R, Turek S, editors. Flux-corrected transport: principles, algorithms, and applications. second ed.. Springer; 2012, p. 67–90.
[41] Grinstein FF, Margolin LG, Rider WJ. Implicit large eddy simulation. Cambridge: Cambridge University Press; 2007.
[42] Benhamadouche S, Laurence D. Global kinetic energy conservation with unstructured meshes. Internat J Numer Methods Fluids 2002;40(3–4):561–71.
[43] Perot JB. Discrete conservation properties of unstructured mesh schemes. Annu Rev Fluid Mech 2011;43(1):299–318.
[44] Veldman AEP. A general condition for kinetic-energy preserving discretization of flow transport equations. J Comput Phys 2019;398:108894.
[45] Verstappen RWCP, Veldman AEP. Symmetry-preserving discretization of turbulent flow. J Comput Phys 2003;187(1):343–68.
[46] Duchon J, Robert R. Inertial energy dissipation for weak solutions of incompressible Euler and Navier–Stokes equations. Nonlinearity 2000;13(1):249.
[47] Coquel F, Le Floch P. Convergence of finite difference schemes for conservation laws in several space dimensions: The corrected antidiffusive flux approach. Math Comp 1991;57(195):169–210.
[48] Hoffman J, Jansson J, Jansson N, De Abreu RV. Towards a parameter-free method for high Reynolds number turbulent flow simulation based on adaptive finite element approximation. Comput Methods Appl Mech Engrg 2015;288:60–74.

[49] Fehn N, Kronbichler M, Lube G. From anomalous dissipation through Euler singularities to stabilized finite element methods for turbulent flows. 2024, Preprint: https://doi.org/10.21203/rs.3.rs-4187657/v1, Accepted to Flow, Turbulence & Combus- tion, 2024.

[50] Hajduk H, Kuzmin D. Bound-preserving and entropy-stable algebraic flux correction schemes for the shallow water equations with topography. In: Eleventh international conference on computational fluid dynamics. 2022, Paper ICCFD11-2022-3003.

[51] Becker R, Hansbo P. A simple pressure stabilization method for the Stokes equation. Commun Numer Methods Eng 2008;24(11):1421–30.

[52] Székelyhidi Jr L, Wiedemann E. Young measures generated by ideal incompressible fluid flows. Arch Ration Mech Anal 2012;206(1):333–66.

[53] Lanthaler S. Computation and analysis of statistical solutions of the incompressible Euler equations (Ph.D. thesis), ETH Zurich; 2021.

[54] Lanthaler S, Mishra S. Computation of measure-valued solutions for the incompressible Euler equations. Math Models Methods Appl Sci 2015;25(11):2043–88, Id/No 2043.

[55] Arun KR, Krishnamurthy A, Lukáčová-Medvid'ová M. Asymptotic preserving finite volume method for the compressible Euler equations: Analysis via dissipative measure-valued solutions. 2024, Preprint: https://arxiv.org/abs/2405.05685 [math.NA].

[56] Breit D, Dodgson A. Space-time approximation of local strong solutions to the 3D stochastic Navier–Stokes equations. Comput Methods Appl Math 2023;24(3):577–97.

[57] Breit D, Prohl A. Numerical analysis of two-dimensional Navier–Stokes equations with additive stochastic forcing. IMA J Numer Anal 2022;43(3):1391–421.

[58] Chaudhary A. Convergence of a spectral method for the stochastic incompressible Euler equations. ESAIM, Math Model Numer Anal 2022;56(6):1993–2019.

[59] Elman H, Silvester D, Wathen A. Finite elements and fast iterative solvers: with applications in incompressible fluid dynamics. Oxford University Press; 2014.

[60] Brandts J, Korotov S, Křížek M. Simplicial partitions with applications to the finite element method. Springer; 2020.

[61] Brezzi F, Pitkäranta J. On the stabilization of finite element approximations of the Stokes equations. In: Efficient solutions of elliptic systems. Notes on numerical fluid mechanics, Vieweg+Teubner; 1984, p. 11–9.

[62] Barrenechea GR, John V, Knobloch P, Rankin R. A unified analysis of algebraic flux correction schemes for convection-diffusion equations. SeMA J 2018;75(4):655–85.

[63] Selmin V. The node-centred finite volume approach: Bridge between finite differences and finite elements. Comput Methods Appl Mech Engrg 1993;102(1):107–38.

[64] Selmin V, Formaggia L. Unified construction of finite element and finite volume discretizations for compressible flows. Internat J Numer Methods Engrg 1996;39:1–32.

[65] Guermond J-L, Popov B. Error estimates of a first-order Lagrange finite element technique for nonlinear scalar conservation equations. SIAM J Numer Anal 2016;54(1):57–85.

[66] Larson S, Thomée V. Partial differential equations with numerical methods. Springer; 2003.

[67] Chen CM, Thomée V. The lumped mass finite element method for a parabolic problem. ANZIAM J 1985;26(3):329–54.

[68] Kato T, Lai CY. Nonlinear evolution equations and the Euler flow. J Funct Anal 1984;56(1):15–28.

[69] Majda A. Compressible fluid flow and systems of conservation laws in several space variables. In: Appl. math. sci., vol. 53, Springer; 1984.

[70] DiPerna RJ. Compensated compactness and general systems of conservation laws. Trans Amer Math Soc 1985;292(2):383–420.

[71] Brenier Y, De Lellis C, Székelyhidi Jr L. Weak-strong uniqueness for measure-valued solutions. Comm Math Phys 2011;305(2):351–61.

[72] Wiedemann E. Weak-strong uniqueness in fluid dynamics. In: Partial differential equations in fluid mechanics. London mathematical society lecture note series, Cambridge University Press; 2018, p. 289–326.

[73] Gwiazda P, Kreml O, Świerczewska-Gwiazda A. Dissipative measure-valued solutions for general conservation laws. Ann de L'Inst Henri Poincaré C, Anal Non Linéaire 2020;37(3):683–707.

[74] Feireisl E, Lukáčová-Medviďová M, Mizerová H. $\mathscr{K}$-convergence as a new tool in numerical analysis. IMA J Numer Anal 2020;40(4):2227–55.

[75] Lukáčová-Medvid'ová M, Rohde C. Mathematical challenges for the theory of hyperbolic balance laws in fluid mechanics: complexity, scales, randomness. Jahresber Dtsch Math- Ver 2024;126(4):283–311.

[76] Frank F, Reuter B, Aizinger V, Hajduk H, Rupp A. FESTUNG: The finite element simulation toolbox for UNstructured grids, version 1.0. 2020, https://github.com/FESTUNG.

[77] Reuter B, Hajduk H, Rupp A, Frank F, Aizinger V, Knabner P. FESTUNG 1.0: Overview, usage, and example applications of the MATLAB / GNU Octave toolbox for discontinuous Galerkin methods. Comput Math Appl 2021;81:3–41.

[78] Anderson R, Andrej J, Barker A, Bramwell J, Camier J-S, Cerveny J, et al. MFEM: A modular finite element methods library. Comput Math Appl 2021;81:42–74.

[79] MFEM: Modular Finite Element Methods [Software]. https://mfem.org.

[80] GLVis: OpenGL Finite Element Visualization Tool. https://glvis.org.

[81] Schroeder PW. Robustness of high-order divergence-free finite element methods for incompressible computational fluid dynamics (Ph.D. thesis), University Goettingen; 2019.

[82] Lube G, Schroeder PW. Implicit LES with high-order H(div)-conforming FEM for incompressible Navier–Stokes flows. In: Boundary and interior layers, computational and asymptotic methods BAIL 2018. LNCSE 135, Springer; 2020, p. 157–70.

[83] Van Groesen E. Time-asymptotics and the self-organization hypothesis for 2D Navier–Stokes equations. Phys A: Stat Mech Appl 1988;148(1–2):312–30.

[84] https://www.cfd-online.com/Wiki/Gresho_vortex.

[85] Gresho PM, Chan ST. On the theory of semi-implicit projection methods for viscous incompressible flow and its implementation via a finite element method that also introduces a nearly consistent mass matrix. Part 2: Implementation. Internat J Numer Methods Fluids 1990;11(5):621–59.